

# On-axis spectroscopy of the host galaxies of 20 optically luminous quasars at $z \sim 0.3$ \*

G. Letawe,<sup>1†</sup> P. Magain,<sup>1</sup> F. Courbin,<sup>2</sup> P. Jablonka,<sup>2,3</sup>  
K. Jahnke,<sup>4</sup> G. Meylan,<sup>2</sup> and L. Wisotzki<sup>5</sup>

<sup>1</sup> Institut d’Astrophysique et Géophysique, Université de Liège, Allée du 6 Août, 17, Sart Tilman (Bat. B5C), B-4000 Liège, Belgium

<sup>2</sup> Laboratoire d’Astrophysique, Ecole Polytechnique Fédérale de Lausanne (EPFL), Observatoire, CH-1290 Sauverny, Switzerland

<sup>3</sup> Observatoire, Université de Genève, CH-1290 Sauverny, Switzerland

<sup>4</sup> Max-Planck-Institut für Astronomie, Königstuhl 17, D- 69117 Heidelberg, Germany

<sup>5</sup> Astrophysikalisches Institut Potsdam, An der Sternwarte 16, D-14482 Potsdam, Germany

22 April 2018

## ABSTRACT

We present the analysis of a sample of 20 bright low-redshift quasars ( $M_B < -23$  and  $z < 0.35$ ) observed spectroscopically with the VLT. The FORS1 spectra, obtained in Multi Object Spectroscopy (MOS) mode, allow to observe simultaneously the quasars and several reference stars used to spatially deconvolve the data. Applying the MCS deconvolution method, we are able to separate the individual spectra of the quasar and of the underlying host galaxy. Contrary to some previous claims, we find that luminous quasars are not exclusively hosted by massive ellipticals. Most quasar host galaxies harbour large amounts of gas, irrespective of their morphological type. Moreover, the stellar content of half of the hosts is a young Sc-like population, associated with a rather low metallicity interstellar medium. A significant fraction of the galaxies contain gas ionized at large distances by the quasar radiation. This large distance ionization is always associated with signs of gravitational interactions (as detected from images or disturbed rotation curves). The spectra of the quasars themselves provide evidence that gravitational interactions bring dust and gas in the immediate surrounding of the super massive black hole, allowing to feed it. The quasar activity might thus be triggered (1) in young gas-rich spiral galaxies by local events and (2) in more evolved galaxies by gravitational interactions or collisions. The latter mechanism gives rises to the most powerful quasars. Finally, we derive mass models for the isolated spiral host galaxies and we show that the most reliable estimators of the systemic redshift in the quasar spectrum are the tips of the  $H\alpha$  and  $H\beta$  lines.

**Key words:** Galaxies: active, stellar content, interactions – techniques: image processing, spectroscopy – Quasars: general

## 1 INTRODUCTION

Close to half a century has passed since the first detailed spectroscopic observations of a quasi-stellar-object (QSO) (Oke 1963; Greenstein & Schmidt 1964), and two decades since the first clear spectroscopic evidence that quasars are located in the centres of much larger stellar envelopes or *host galaxies* (Boroson et al. 1984). After this pioneering spectroscopic work, most studies have concentrated on imaging, attempting to measure the shape and the luminosity of

quasar host galaxies (e.g., Bahcall et al. 1997; Dunlop et al. 2003). With better image processing techniques, it has become possible to derive information about the stellar content of quasar hosts using multicolour imaging (Rönnback et al. 1996; Jahnke et al. 2004; Sanchez et al. 2004), but very little effort has been spent on genuine deep spectroscopy, mainly because of the difficulty to accurately decontaminate the galactic spectrum from the light of the central quasar.

The quasar-host separation problem has been circumvented, at least in part, in three ways. One is to restrict oneself to samples of obscured quasars (Kauffmann et al. 2003), with the obvious drawback that samples built in that way are biased, and that there is no easy way to accurately recover the unobscured quasar luminosity. Another technique is to carry out off-axis spectroscopy: the spectra are ob-

\* Based on observations made with the ESO Very Large Telescope Unit 1 (ANTU/UT1) at ESO Paranal Observatory, Chile, under program IDs 65.P-0361, and 66.B-0139.

† E-mail: gletawe@ulg.ac.be

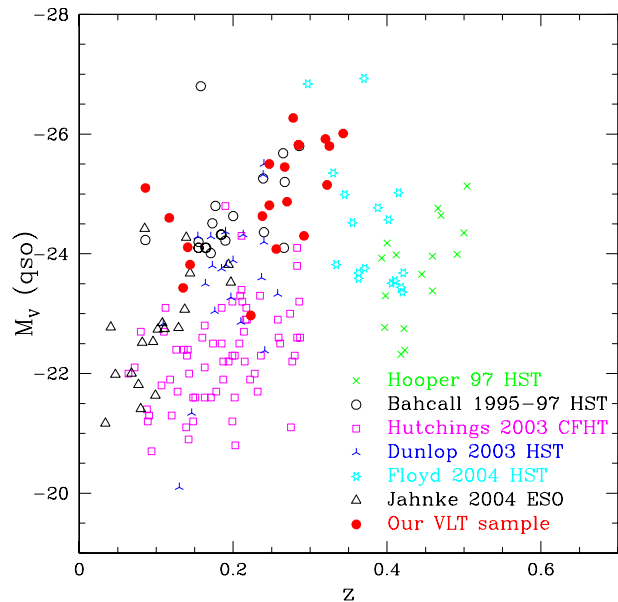


**Figure 1.** Location of our quasar sample in the absolute magnitude vs. redshift plane, compared with other samples observed in imaging either with the *HST* or from the ground (CFHT, ESO).

tained with the slit of the spectrograph located a few arcseconds away from the quasar (e.g., Hutchings & Crampton 1990; Nolan et al. 2001; Miller & Sheinis 2003). However, residual contamination by the quasar remains difficult to remove completely, the velocity information on the host is lost, and only the external parts of the host can be studied. Finally, the 1D template-spectra of non-active galaxies can be used as a basis to perform eigenvector decomposition (Vanden Berk et al. 2006). The latter method is efficient in drawing general conclusions using very large numbers of objects, but relies on a restricted number of eigenspectra. This prevents the discovery of unexpected spectral features, e.g., due to the specific spatial distribution of the gas in each galaxy, to the starburst activity, or to winds and jets escaping from the central AGN.

In the present work, we take advantage of a new approach, where the quasar spectra are taken on-axis, i.e. with the slit lying directly across the nuclear point source. Our quasar-host separation technique relies on a spatial deconvolution of the spectra, using the spectra of neighbouring PSF stars. This method has already been exploited in three previous papers (Courbin et al. 2002; Letawe et al. 2004; Magain et al. 2005) and allows to go beyond previous studies: 1- the spectral properties of the hosts can be determined down to the central kpc; 2- the stellar and gaseous contributions to the total spectrum can be accurately separated, which is not the case in multicolour imaging; 3- no prior assumption on the host, neither spectral nor morphological, is necessary during the deconvolution process; 4- the velocity curve of the host around its central quasar can be measured.

Recent studies have argued that luminous quasars reside in massive elliptical galaxies (Dunlop et al. 2003) with globally old stellar populations, but with slightly bluer colours than their quiescent counterparts, indicative of an additional younger stellar component (Kauffmann et al.

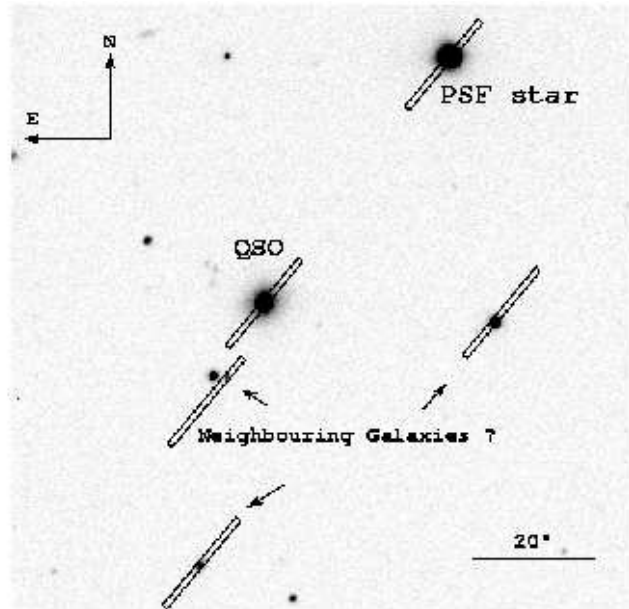


**Figure 2.** Example of a MOS mask used to carry out the FORS1 observations, for the quasar HE1503+0208. One slitlet ( $19 \times 1$  arcsec) is positioned on the quasar, and several others on PSF stars. The remaining slitlets are used to obtain the spectra of neighbouring galaxies.

2003; Jahnke et al. 2004; Vanden Berk et al. 2006). We show that these general conclusions should be taken with caution, as important information is lacking from their data, such as separation of the gas and stars, velocity fields, gas ionization, . . . In particular, we investigate how the central AGN affects the evolution of the whole galaxy by carrying out a comparative study between samples of galaxies with and without quasars. We compare their stellar populations and the ionization state of their Interstellar Medium (ISM). Whenever possible, we infer the dynamical mass of the host galaxies and we trace distortions of their velocity field due to past or present interactions with nearby companions.

Our work is a first step towards a larger spectroscopic study of quasar hosts aimed at understanding why some galaxies are active while others are not. Many studies have characterized the morphology of the hosts, but the morphology alone does not reflect the actual stellar and gaseous content of the hosts. The aforementioned blue colours of quasar hosts confirm that their evolution does not follow a classical path. It is thus important to understand how their stage of evolution is linked to the nuclear activity. Because of the complexity and because of the variety of physical phenomena at work in quasars and their host galaxies, the observational solutions of this puzzle can only come from combined spectroscopic and imaging studies.

In Section 2, we present our sample of 20 low-redshift optically luminous quasars. In Sections 3 and 4 we describe the observations and data processing. Imaging is treated in Section 5, while we give in Section 6 an overview of the spectral analysis, further detailed in Section 7. Section 8 is devoted to the dynamics of quasar hosts and to the detection of gravitational interactions with companions, while Section 9 studies the links between the nuclear and host properties. Fi-

nally, Section 10 establishes the relation between the redshift of the quasars and that of their host galaxy. Throughout the paper, we adopt the following cosmological parameters:  $H_0 = 65 \text{ km s}^{-1} \text{ Mpc}^{-1}$ ,  $\Omega_m = 0.3$  and  $\Omega_\Lambda = 0.7$ .

## 2 THE SAMPLE

Our quasar sample is selected from the flux-limited Hamburg-ESO Survey (HES) (Wisotzki et al. 2000). The HES is designed to detect optically luminous quasars and Seyferts 1 in the Southern hemisphere, with optical magnitudes  $13 < B < 17.5$  and redshifts  $z < 3.2$ . The classification of the candidates as quasars is made spectroscopically from the broad-band features. Out of this sample, we selected the intrinsically luminous quasars, with absolute magnitude  $M_B < -23$  and redshift  $z < 0.35$  (this redshift limit is set so that the  $H\alpha$  line stays in our useful spectral range). From the 32 QSOs matching these criteria, we could observe 20. No spectral or morphological selection of the object was applied prior to the observations. The only relevant factor in our choice of an object was its visibility at the time of the observing runs. Table 1 gives the main characteristics of our sample. Figure 1 shows the location of all our objects in the absolute magnitude vs. redshift plane and compares them with previous studies that all use imaging rather than spectroscopy (e.g. Floyd et al. 2004; Dunlop et al. 2003; Bahcall et al. 1997). Our sample concentrates on the brightest part of the quasar luminosity function and at rather low redshift. Its characteristics compare well with those of Floyd et al. (2004) and Bahcall et al. (1997).

## 3 OBSERVATIONS

### 3.1 Spectroscopy

Our spectroscopic observations were obtained with the ESO Very Large Telescope (VLT) and the FORS1 instrument in Multi Object Spectroscopy (MOS) mode. The data were acquired during two observing runs, in April and November 2000. All objects were observed with 3 medium resolution grisms (G600B, G600R and G600I), thus covering the full optical spectral range 3500-9000Å. The seeing varied between 0.5 and 2.2 arcsec (see Table 1), and the pixel scale was 0.2 arcsec, using the standard resolution collimator. The slitlet ( $19 \times 1$  arcsec) of the MOS mask closest to the optical axis was centred on the quasar itself (on-axis). Several slitlets were used to obtain the spectra of PSF stars with the same spectral range as the quasar, which is crucial for subsequent deconvolution of the data using the spectroscopic version of the MCS algorithm (Magain et al. 1998; Courbin et al. 2000, see Section 4). The remaining slitlets were placed on galaxies in the field, in order to look for possible companions, groups or clusters (see Section 8.2). We show in Fig. 2 a typical MOS mask configuration for the 5 slitlets closest to the quasar. As the slits are parallel, the orientation of the mask relative to the major axis of the host galaxy (when visible prior to deconvolution) is imposed by the necessity to observe simultaneously at least one PSF star (in fact two for the majority of the fields observed) with the same spectral coverage as for the quasar.

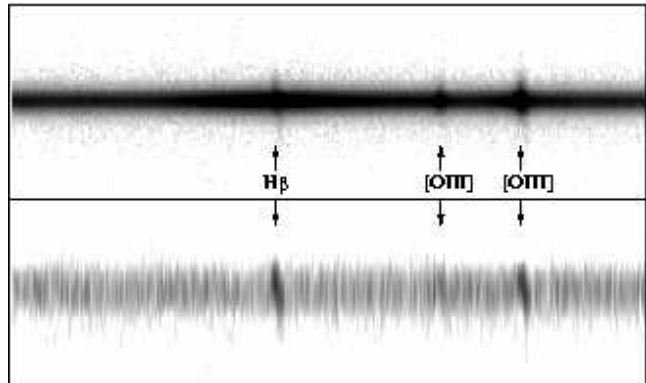


**Figure 3.** Example of spectra decomposition using the MCS algorithm, for the  $z = 0.223$  quasar HE 2345-2906. The spectrum shown here spans the wavelength interval 5800-6250 Å. The top panel displays the original data with the VLT spectrum of the quasar plus host galaxy. The bottom panel is the result of the decomposition, where only the 2D-spectrum of the host is shown. The narrow emission lines of the host can be traced down to the centre of the galaxy. The height of each panel is 19 arcsec.

The reduction of the spectra was carried out with the standard IRAF packages, leading to bias-subtracted, flat-fielded, and sky-subtracted spectra. The wavelength calibration was done using Ne-Ar-He spectra obtained in the same slit configuration as the observations. It has been performed on the two dimensional spectra in order to correct for slit curvature and to ease the sky subtraction. All spectra were rebinned to a pixel scale of 1 Å in the spectral direction and 0.2 arcsec in the spatial direction. When several exposures were available in a given grism, they were combined into one deeper spectrum using a cosmic-ray rejection algorithm. Spectroscopic standard stars were observed during the two runs in order to allow for an accurate flux calibration.

### 3.2 Imaging

The imaging part of the sample was limited to acquisition images obtained during the spectroscopic runs, with 30s exposure time through the  $R$  or  $V$  filters. The seeing spanned a broad range, 0.5 to 1.5 arcsec. The pixel scale is 0.2 arcsec, as in the spectra. In one case the QSO is saturated (HE 0441-2826). The reduction of all images was performed with the IRAF package. It consisted in bias subtraction, flat-fielding and sky subtraction. Standard stars were also observed in each run for magnitude determination.

## 4 DECONVOLUTION OF THE DATA

The whole sample of 2D spectra and images has been deconvolved using the MCS algorithm (Magain et al. 1998) and its extension to spectra (Courbin et al. 2000). In the MCS deconvolution algorithm, the final resolution is chosen by the user, but is constrained to be compatible with the sampling of the deconvolved data. In this way, the resolution of the processed data is improved but not infinitely high, and the deconvolved data do not show any of the undesirable “deconvolution artefacts” often found using other algorithms. In addition, the MCS method is particularly well suited to the

**Table 1.** Our QSO sample sorted by increasing right ascension: (1-) Object name, (2-) redshift determined from the H $\alpha$  emission line of the quasar (see Section 10), (3-) integrated absolute  $B$  magnitude from the HES catalogue, (4-5) absolute  $V$ -magnitude for the quasar and host as measured from our VLT observations, (6-) observing run (A = April 2000; B = November 2000), (7-) Galactic extinction from Schlegel et al. (1998), (8-9) seeing value and exposure time for each grism (G600B, G600R, G600I), (10-) host morphology as determined from other studies (see Section 5) and interaction signs. D stands for disc dominated, E for elliptical, U for undefined, the number coding stands for: 0 = no interaction signs, 1 = close companion outside the galaxy, 2 = tails, 3 = merger, (11-) quasar properties: objects with radio emission are indicated by R (from NVSS), but only HE1302-1017 is radio-loud. Narrow line quasars are labelled NL (see Section 9).

| Object name  | z(H $\alpha$ )<br>quasar | M $_B$ (tot)<br>HES | M $_V$ (QSO)<br>VLT | M $_V$ (host)<br>VLT | Run | E( $B - V$ ) | Seeing<br>arcsec: $B, R, I$ | $t_{exp}$<br>seconds: $B, R, I$ | Gal    | QSO  |
|--------------|--------------------------|---------------------|---------------------|----------------------|-----|--------------|-----------------------------|---------------------------------|--------|------|
| HE 0132-4313 | 0.237                    | -24.37              | -24.63              | -22.63               | B   | 0.017        | 0.65-0.71-0.67              | 3000-1800-1800                  | U, 0   | NL   |
| HE 0203-4221 | 0.319                    | -24.88              | -25.92              | -23.10               | B   | 0.014        | 0.71-0.75-0.60              | 3000-1800-1800                  | U, 2   |      |
| HE 0208-5318 | 0.344                    | -24.76              | -26.01              | -23.00               | B   | 0.026        | 0.61-0.50-0.50              | 3000-1800-1800                  | U, 0   |      |
| HE 0306-3301 | 0.247                    | -24.32              | -24.81              | -22.41               | B   | 0.014        | 0.68-0.66-0.86              | 3000-1800-1800                  | D, 2,3 |      |
| HE 0354-5500 | 0.267                    | -24.70              | -25.45              | -23.47               | B   | 0.016        | 0.52-0.67-0.48              | 3600-1800-1800                  | D, 3   |      |
| HE 0441-2826 | 0.155                    | -24.62              | -                   | -                    | B   | 0.035        | 0.74-0.47-0.53              | 3000-1800-2400                  | E, 0   | R    |
| HE 0450-2958 | 0.286                    | -25.24              | -25.82              | -                    | B   | 0.015        | 0.54-0.67-0.57              | 3600-1800-1800                  | U, 1   | NL,R |
| HE 0530-3755 | 0.293                    | -24.07              | -24.30              | -20.70               | B   | 0.027        | 0.70-0.68-0.65              | 3000-1800-1000                  | U, 1,2 |      |
| HE 0914-0031 | 0.322                    | -25.01              | -25.15              | -22.02               | A   | 0.035        | 2.06-2.11-2.24              | 1200-1200-1200                  | D, 0   |      |
| HE 0956-0720 | 0.326                    | -24.79              | -25.80              | -23.04               | A   | 0.055        | 0.53-0.65-0.59              | 1200-1200-1200                  | U, 0   |      |
| HE 1009-0702 | 0.271                    | -24.28              | -24.87              | -22.94               | A   | 0.033        | 0.69-0.64-0.70              | 1800-1800-1800                  | D, 0   | NL   |
| HE 1015-1618 | 0.247                    | -25.13              | -25.50              | -22.55               | A   | 0.078        | 1.20-0.92-1.01              | 1200-1200-1200                  | D, 0   |      |
| HE 1029-1401 | 0.086                    | -25.07              | -25.10              | -22.53               | A   | 0.067        | 1.61-1.54-1.94              | 1200-1200-1200                  | E, 3   | R    |
| HE 1228+0131 | 0.118                    | -24.33              | -24.60              | -21.44               | A   | 0.019        | 0.91-0.76-0.72              | 1200-1200-1200                  | E, 0   | NL   |
| HE 1302-1017 | 0.278                    | -26.15              | -26.27              | -23.40               | A   | 0.043        | 0.60-0.60-0.50              | 2400-1800-1800                  | U, 3   | R    |
| HE 1434-1600 | 0.144                    | -24.34              | -23.82              | -22.87               | A   | 0.126        | 0.58-0.60-0.49              | 1200-1200-1200                  | E, 1   | R    |
| HE 1442-1139 | 0.257                    | -23.81              | -24.08              | -23.23               | A   | 0.079        | 0.98-1.20-1.10              | 1200-1200-1200                  | D, 0   |      |
| HE 1503+0228 | 0.135                    | -23.02              | -23.43              | -22.78               | A   | 0.05         | 0.60-0.68-0.72              | 1200-1200-1200                  | D, 0   |      |
| HE 2258-5524 | 0.141                    | -23.71              | -24.11              | -23.11               | B   | 0.013        | 0.88-0.70-0.76              | 3000-1800-1800                  | U, 3   | NL   |
| HE 2345-2906 | 0.223                    | -23.09              | -22.97              | -22.84               | B   | 0.019        | 0.86-0.83-0.67              | 3000-1500-1500                  | D, 0   |      |

quasar host studies because of its ability to separate point sources (here the quasars) from diffuse ones (the host galaxies). Taking advantage of the availability of several stars to construct the PSF, we could as well subsample our deconvolved spectra and images, leading to a final sampling of 0.1 arcsec per pixel.

The deconvolution of spectra with MCS, as every deconvolution procedure, is highly sensitive to the accuracy of the PSF. Poor deconvolution results are always associated with problems in the PSF construction. Several weaknesses of the process account for uncertainties sometimes found in the deconvolution results and difficulties in separating both components. (1) The stars are often not bright enough in the bluer part of the G600B grism, in comparison to the quasar. This introduces extra noise at the shortest wavelengths in the deconvolved spectra. (2) The orientation and angular separation of the slits being imposed by the geometry of the mask (see Fig. 2), it may happen that parts of the PSF wings are lost on one side because the star could not be centred on the slit. (3) The spectral types of the stars can influence the quality of the PSF, smoother stellar spectra being preferred to spectra with many strong absorption lines. (4) Finally, the slight variation of the PSF profile across the field is minimized by taking the stars closest to the quasar for PSF construction or by the use of several stars on both sides of the quasar to average the profile variation. For 85 % of the objects in our sample, the simultaneous observation of several stars allows to construct reliable PSFs. The main characteristics of the PSF stars are summarized in Table 2.

Figure 3 shows an example of deconvolution. The reduced spectrum is shown on the top panel of the figure,

while the 2D-spectrum of the host galaxy alone is shown in the bottom panel. The MCS method is used here essentially in order to efficiently separate the nuclear and diffuse components of the data rather than for sharpening the data in the spatial direction. Depending on the signal-to-noise ratio (S/N), this may result in some smoothing of the extended source or, in any case, in no significant gain in resolution. Figure 3 nevertheless clearly shows that no significant residual flux from the quasar is left in the spectrum of the host galaxy. For example, the spectrum of the host does not display any residual from the broad quasar emission lines.

Once the data are deconvolved, we extract 1D spectra by integrating fluxes over the spatial direction, in the quasar spectrum and in the host spectrum. The final atlas of quasar and host spectra is shown in Fig. 19.

#### 4.1 Estimate of the uncertainties on quasar/host separation

While the outcome of the deconvolution process shows no traces of contamination from the quasar light in the host spectrum (as illustrated by Fig. 3), it nevertheless appears useful to estimate the maximum effects an imperfect separation between host galaxy and nuclear spectra may have on the various results presented hereafter.

For this purpose, we adopt a very conservative approach, deciding not to trust the quasar/host separation given by the deconvolution process, and arbitrarily changing the magnitude of the quasar spectrum to be subtracted from the total (quasar+host) spectrum, until the shape of the host spectrum shows clear signs of (either positive or

**Table 2.** Quantitative estimates of uncertainties in the deconvolution process and characteristics of the PSF stars used for deconvolution. We give here the percentage of the quasar flux that can be added to (+%) or subtracted from (-%) the galactic spectra before a clear nuclear signature appears (see text and Fig. 19), the angular separation  $\theta$  between the quasar and the PSF star(s) and indicative PSF star(s) magnitude(s) in the B band, to be compared to the quasar apparent magnitude.

| Object name  | +%  | -%  | $\theta$ (min:sec) | B(PSF)    | B(QSO) |
|--------------|-----|-----|--------------------|-----------|--------|
| HE 0132–4313 | 1   | 1   | 1:09/2:16          | 17.8/16.2 | 16.4   |
| HE 0203–4221 | 0.5 | 0.2 | 1:02/2:05          | 14.6/13.8 | 16.0   |
| HE 0208–5318 | 1   | 1   | 1:11/1:35          | 16./14.8  | 16.1   |
| HE 0306–3301 | 1   | 1   | 1:34/2:02          | 16.5/15.4 | 15.3   |
| HE 0354–5500 | 2   | 0.5 | 2:22/1:41          | 16.1/17.  | 15.6   |
| HE 0441–2826 | 1   | 0.6 | 1:53/2:14          | 18./14.   | 15.2   |
| HE 0450–2958 | 0.5 | 0.2 | 1:59               | 15.3      | 14.8   |
| HE 0530–3755 | 0.8 | 0.5 | 1:49/2:03          | 14.8/16.6 | 16.1   |
| HE 0914–0031 | 2   | 1   | 1:04               | 16.       | 16.9   |
| HE 0956–0720 | 1   | 1   | 1:12 1:43          | 15.2 16.9 | 15.2   |
| HE 1009–0702 | 1.5 | 1   | 1:29/1:22          | 15.9/16.3 | 15.9   |
| HE 1015–1618 | 1   | 1   | 1:46/0:55          | 18.5/18.7 | 15.2   |
| HE 1029–1401 | 1   | 0.5 | 1:23               | 15.6      | 13.5   |
| HE 1228+0131 | 0.8 | 1   | 2:06               | 14.7      | 14.4   |
| HE 1302–1017 | 0.5 | 0.2 | 1:01/1:08          | 16./15.7  | 14.5   |
| HE 1434–1600 | 3   | 2   | 1:39               | 17.8      | 14.8   |
| HE 1442–1139 | 5   | 2   | 0:36/1:46          | 16.5/16.9 | 15.5   |
| HE 1503+0228 | 3   | 2   | 0:51               | 16.1      | 15.8   |
| HE 2258–5524 | 2   | 1   | 2:57               | 13.6      | 14.7   |
| HE 2345–2906 | 4   | 2   | 0:39/1:08          | 17.2/16.7 | 16.1   |

negative) contamination. We thus determine the limits for over- or undersubtraction of the nuclear spectrum.

In practice, we concentrate on the spectral region containing the  $H\beta$  and  $[OIII]$  lines, as these spectral features are of prime importance for the derivation of the galactic properties.

The limit of oversubtraction of the quasar spectrum is set, for each object separately, when one of the following conditions is met: (1) the 2D host spectrum presents a depression in the centre, (2) a broad  $H\beta$  component appears in absorption on the integrated host spectrum, (3) the continuum flux of the host reaches zero. The limit of undersubtraction of the nuclear component is set when: (1) the spatial profile of the host spectrum clearly shows a central point source, or (2) a broad  $H\beta$  or  $H\gamma$  emission appears in the integrated host spectrum.

Such error bars, set when visual inspection clearly shows a problem, should be considered as roughly amounting to 2  $\sigma$  (which means that we estimate to be able to detect such a wrong subtraction in 95% of the cases). The percentage of nuclear flux that has to be added to reach the limit of oversubtraction or removed to detect an undersubtraction is given, for each object, in Table 2.

Each galactic property derived hereafter has been evaluated from the deconvolved spectra *and* from the associated upper and lower limit spectra derived as explained above, thus allowing a quantitative estimate of the very conservative uncertainties related to the deconvolution (or, rather, to the quasar/host separation). These upper and lower limit spectra are represented as dotted curves on the atlas of Fig. 19

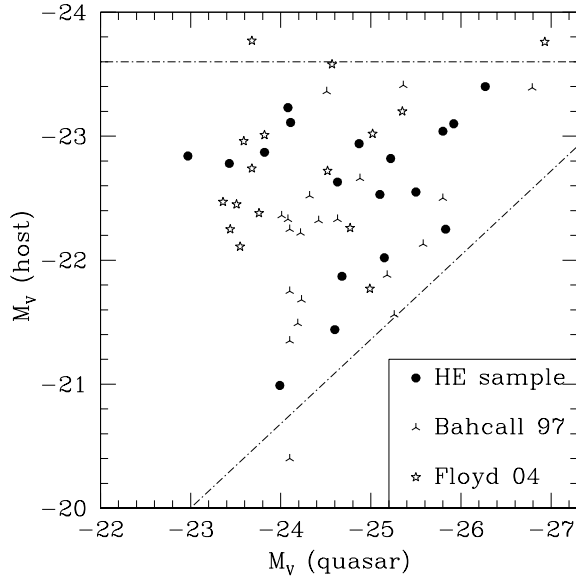


**Figure 4.** Absolute  $M_V$  magnitude of the host galaxies versus absolute  $M_V$  magnitude of the quasar. For comparison, we also plot the two samples of quasars covering the same luminosity range, from Floyd et al. (2004) and Bahcall et al. (1997), converted to our cosmology. The dotted lines show the envelope discussed in the text.

## 5 IMAGE ANALYSIS

A short 30-seconds  $R$  or  $V$  acquisition image was taken before a long spectroscopic exposure. Even though these images are of low  $S/N$  and were not meant to be used for scientific purposes, they are generally good enough to determine some basic properties of the quasars and of their hosts. We deconvolved all the available images and used them in order to determine the magnitudes of the quasar and of the host, and to unveil any obvious sign of interaction such as tails or companions. Recent *HST*/ACS imaging of some of our objects actually confirms that the shapes given by the deconvolution of these images are accurate enough for that purpose. Two dimensional fitting on these low  $S/N$  data remains unfortunately hazardous.

Figure 5 shows the deconvolved images of the quasar hosts after removal of the quasar itself. HE 0441-2826 is missing because the quasar light reached the saturation of the detector. The host images are used to measure the apparent magnitude of the host galaxies from aperture photometry. We then compute absolute magnitudes (Eq. 1) taking into account the K-correction between the  $R$  (or  $V$ ) filter and the restframe  $V$ -band ( $RV = R_{\text{obs}} - V_{\text{rf}}$ ). This is done without any assumption on the nature of the hosts since we compute their integrated fluxes over the appropriate wavelength bands, directly from our VLT FORS1 spectra. The computations can be summarized as follows:

$$\begin{aligned}
 M_V &= m_R - 5 \log d + 5 - A - 2.5 \log(1+z) - RV \\
 m_R &= m_{R_0} - 2.5 \log(F_R) - a\tau
 \end{aligned} \tag{1}$$

where  $d$  is the distance to the object in parsecs, according to the adopted cosmology,  $A$  the Galactic extinction (from Schlegel et al. 1998),  $z$  is the redshift,  $F_R$  is the

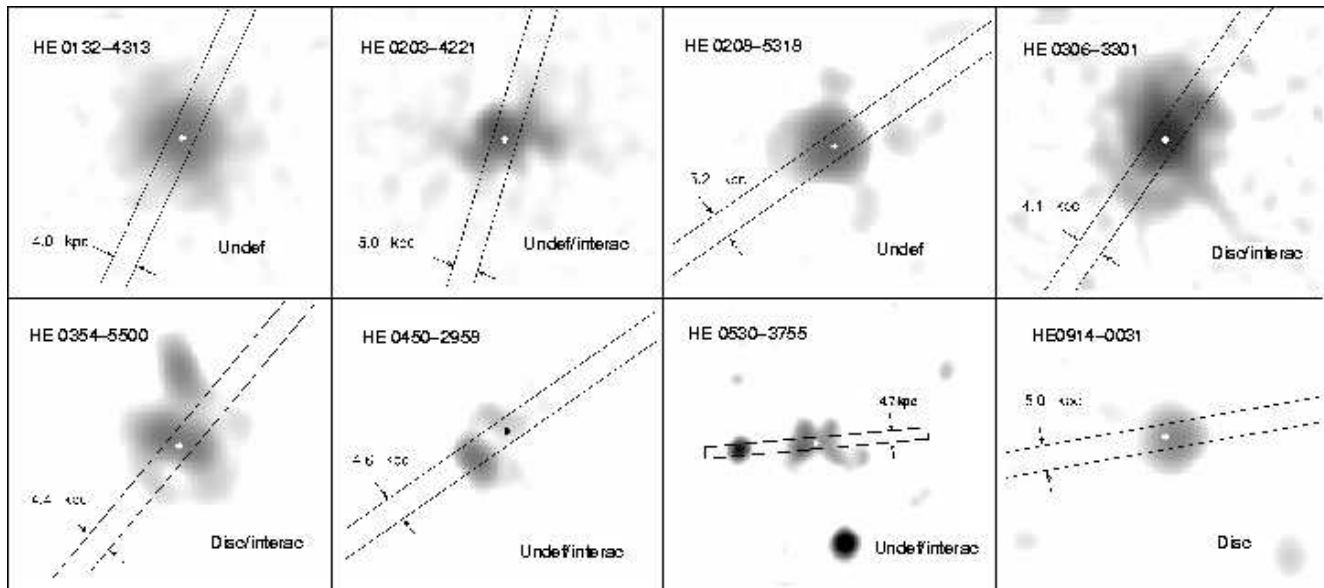


**Figure 5.** Deconvolved VLT images of the host galaxies, in the  $R$ -band (HE 0132-4313, HE 0203-4221 and HE 0914-0031) or in the  $V$ -band (HE 0208-5318, HE 0306-3301, HE 0354-5500, HE 0450-2958 and HE 0530-3755). The quasar light has been removed from these images, which are displayed in a logarithmic intensity scale. Crosses indicate the location of the quasar. The 1 arcsec-wide slits used in spectroscopy are overplotted, and their physical scale on the sky is indicated. Global morphologies are not estimated from these images but are derived following a 2D isophotal fitting of near-IR and/or *HST*/*ACS* data from other studies (see Table 3 in Section 5). In each case we indicate possible signs of interactions, as can be spotted from images and from the radial velocity curves described in Section 8.1. All images are 12 arcsec-wide, except HE 0530-3755 which is 24 arcsec on a side. The intensity cuts are chosen to optimize the contrast and are not identical in all the images. North is up and East to the left.

observed  $R$ -band flux,  $a$  is the airmass,  $\tau$  the atmospheric optical depth, and  $m_{R_0}$  is the zero point determined from the observation of standard stars.

The quality of the deconvolutions can be checked by inspecting the “residual maps”, as defined in Magain et al. (1998). These maps are the absolute differences between the data and the deconvolved images, reconvolved with the PSF, and in units of the photon noise per pixel. A successful deconvolution must show a flat residual map, equal to 1 on average. Based on these residual maps and on numerical simulations, we estimate that the quasar-host decomposition of our VLT acquisition images is accurate to 0.01 mag. However, given that the angular scale of the PSF is similar to that of the bulge component, part of the host flux might be left in the quasar light. This may introduce a systematic underestimate of the flux in the host, especially in cases where it has a compact bulge, which may be difficult to separate from the point source. The magnitudes given in Table 1 are not corrected for such systematic errors. For this reason, we avoid any interpretation relying on host magnitudes alone. However, Fig. 4 shows that our absolute magnitudes for hosts and nuclei are consistent with other studies in the same luminosity range (Bahcall et al. 1997; Floyd et al. 2004) and are useful as a guide to compare our sample with others. While no obvious correlation is apparent between the host and quasar intrinsic luminosity, the points are all located inside an envelope, shown by the dotted lines in Fig. 4. The existence of this envelope suggests that, for a given host magnitude, there is a maximum nuclear luminosity. This was already observed in earlier studies, e.g. by Floyd et al. (2004) or Jahnke et al. (2004), and is explained by the black hole mass - bulge mass relation (McLure & Dunlop 2002):

for a given bulge mass (and hence bulge luminosity), the black hole mass is roughly fixed and the luminosity of the nucleus is more or less limited to the Eddington luminosity (see Section 9.3).

Several objects in the sample had been previously observed by various teams. Kuhlbrodt (2003) and Jahnke et al. (2004) observed some of the objects with the ESO 3.5m New Technology Telescope in the near-IR, and decomposed the data into point sources plus 2D analytical profiles for the hosts (exponential disc or de Vaucouleurs). Two objects, HE 1302-1017 and HE 1029-1401, were also observed with *HST* by Bahcall et al. (1997) and classified as elliptical, both with small close companions. HE 0956-0720 was classified as a disc by Percival et al. (2001). Our recent *HST*/*ACS* images of several objects in the sample has also allowed to detect obvious spiral arms in four hosts, namely HE 0306-3301, HE 0354-5500, HE 1503+0228 and HE 2345-2906 (Letawe et al., in prep). Table 3 gives a summary of the morphological characterizations available, while the adopted morphology is given in Table 1.

## 6 OVERVIEW OF THE SPECTRAL ANALYSIS

Because of the extreme diversity in the gas and stellar contents of quasar host galaxies, the amount of scientific information that can be extracted from our images and spectra is variable from object to object. Most of the analyses proposed in the present work are performed only on subsamples presenting similar characteristics, such as the presence of emission or absorption lines, or the presence of a measur-

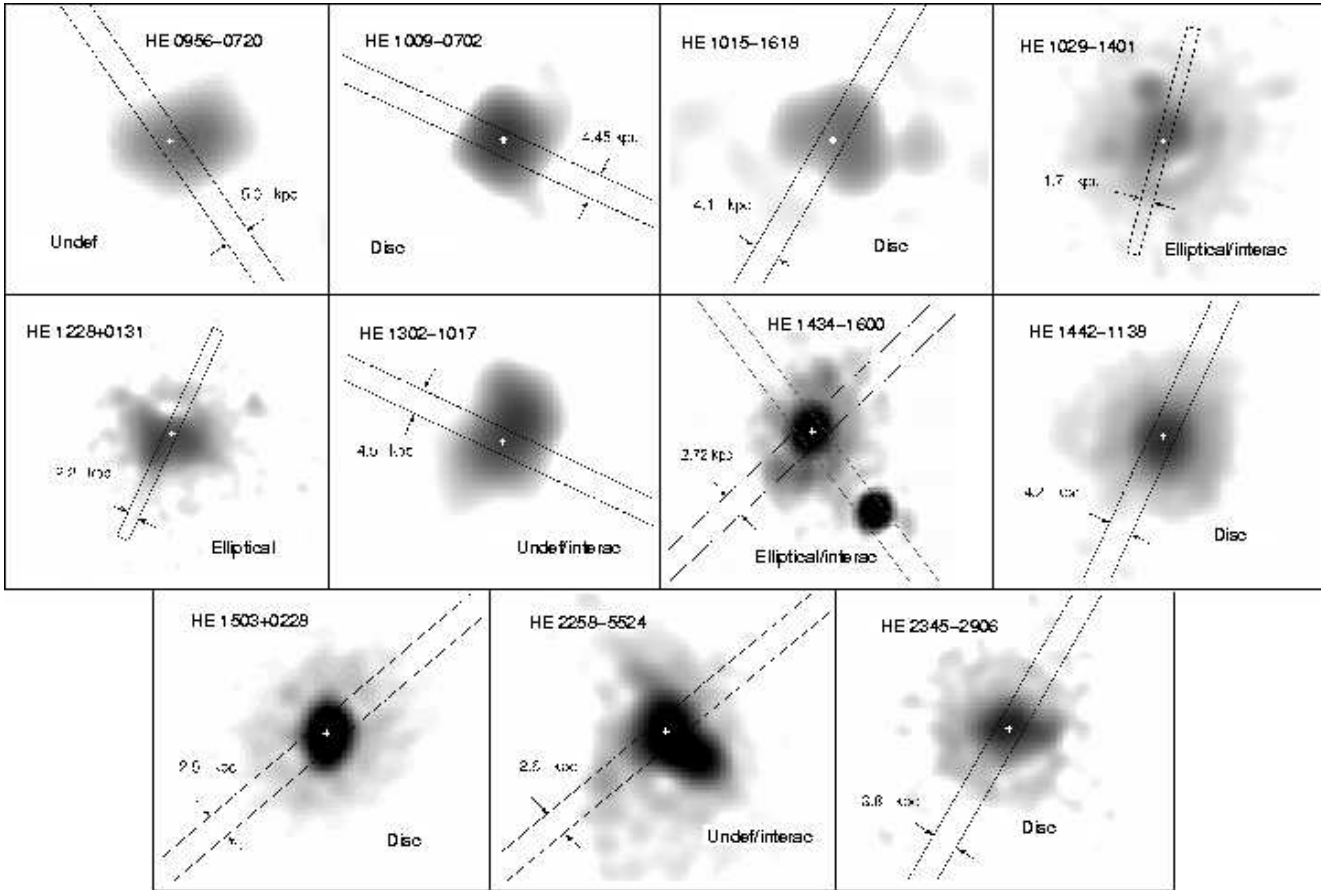


**Figure 5** – *continued* All images are in the  $R$  filter. All images are 12 arcsec-wide, except HE 1029-1401 and HE 1228+0131 that are 24 arcsec-wide. North is up and East to the left. HE 1434-1600 was re-observed with a different slit orientation in order to get the spectrum of a companion galaxy at the same redshift (Letawe et al. 2004).

able velocity field. We summarize in Table 4 which types of measurements were possible for each object.

In spectroscopy, three objects have poor quasar-host separation, either because the quasar reaches the non-linear regime of the detector (1 object, HE 1228+0131), or because of poor PSF determination (2 objects, HE 0956-0720 and HE 1015-1618). However, even with such defects, we would be able to detect galactic emission lines if they were sufficiently prominent and extended. For the three object, we do not detect any underlying emission lines. These hosts are therefore very compact or gas-poor galaxies.

Among the 17 remaining objects, 16 display gas emission lines. For those, we determine the ionisation source of the gas. We classify 9 galaxies as “HII galaxies”, i.e. with gas mainly ionized by stars (Section 7.2), and estimate the star formation rates for these hosts as well as their mean metallicities. The methods we use in order to determine these parameters rely on the gaseous properties of the HII regions only (Sections 7.3 and 7.4).

Twelve host galaxies have spatially extended emission lines, that we use to measure their velocity fields as described in Section 8.1. Among them, 5 are symmetrical about the central quasar and are good candidates for mass modelling through the rotation curves (Section 8). As a by-product, those five regular galaxies give the opportunity to compare the redshift of the object as deduced from the quasar emis-

sion lines and as obtained using the emission lines of the host (Section 10).

Fifteen galaxies out of the 17 that can be analysed exhibit measurable absorption lines that we use to infer the stellar content of the hosts (Section 7.1). We correlate the Lick indices measured on the absorption lines with the Nucleus-to-Host ratios ( $N/H$ ) determined in our VLT images, and find that the absorption lines are detected only in galaxies with  $N/H \lesssim 15$ . This converts to a limit of about  $N/H \leq 45$  in the continuum of the spectra, because of the larger impact of slit losses on the host than on the quasar. We are therefore not able to measure the stellar population of the galaxies with the highest  $N/H$ , including the peculiar object HE 0450-2958 for which no continuum is detected at all (Magain et al. 2005).

Finally, we analyse in Section 9 the quasar spectra themselves and measure some of their main physical properties such as luminosity, mass of the central black hole and accretion rate.

## 7 STELLAR AND GAS CONTENT

We can use our host spectra in order to carry out a comparative study of the gaseous and stellar contents in active and quiescent galaxies. Prior to the analysis, let us note

**Table 3.** Summary of the hosts morphological types and stellar populations. In each column an “E” indicates an elliptical galaxy, “D” stands for disc and “U” for undefined. (1-) Object name, (2-Lit) morphology according to Bahcall et al. (1997) and Percival et al. (2001), (3-NIR) near-IR morphology (Kuhlbrodt 2003; Jahnke et al. 2004), (4-HST) *HST*/ACS F606W morphology from our own ongoing program, (5-Dyn) morphology as derived from the velocity curve of the host (“no D” means that a rotating disc is ruled out), (6-) stellar population from Section 7.1: “Y” for young spiral-like population, “O” for old elliptical-like population, and “I” for intermediate age population. HE 0450-2958 is not classified because no host is detected.

| Object name  | Lit. | NIR | HST | Dyn. | Stell. pop. |
|--------------|------|-----|-----|------|-------------|
| HE 0132-4313 | -    | -   | -   | D    | I           |
| HE 0203-4221 | -    | -   | -   | U    | Y           |
| HE 0208-5318 | -    | -   | -   | -    | Y           |
| HE 0306-3301 | -    | E?  | D   | U    | Y           |
| HE 0354-5500 | -    | -   | D   | U    | Y           |
| HE 0441-2826 | -    | E   | -   | -    | Y           |
| HE 0450-2958 | -    | -   | -   | -    | -           |
| HE 0530-3755 | -    | D?  | -   | -    | -           |
| HE 0914-0031 | -    | D   | -   | D    | Y           |
| HE 0956-0720 | D    | E   | -   | -    | -           |
| HE 1009-0702 | -    | D   | -   | D    | Y           |
| HE 1015-1618 | -    | D   | -   | -    | -           |
| HE 1029-1401 | E    | E   | -   | no D | O           |
| HE 1228+0131 | -    | E   | -   | -    | -           |
| HE 1302-1017 | E?   | D?  | -   | U    | Y           |
| HE 1434-1600 | -    | E   | E   | no D | O           |
| HE 1442-1139 | -    | D   | -   | -    | I           |
| HE 1503+0228 | -    | D   | D   | D    | Y           |
| HE 2258-5524 | -    | -   | -   | U    | I           |
| HE 2345-2906 | -    | -   | D   | D    | Y           |

that for several objects, the galactic  $H\alpha$  emission line is not perfectly separated from the quasar emission because of the combination of (1) the overcrowding of atmospheric lines in this spectral region for objects with the highest redshifts and, with a smaller impact, (2) the very high nucleus-to-host flux ratio in this wavelength range ( $N/H$  up to 180). As a consequence, the determination of the amount of reddening in the host galaxy, as well as other measurements involving  $H\alpha$  fluxes and Equivalent Widths (EWs), are not accurate for all objects in the sample. For this reason we present all our results without any correction for dust extinction. This has little influence on most of the characteristics of our host spectra, as we carefully select the estimators of the various galactic properties analysed here to be as independent on extinction as possible.

### 7.1 Stellar content

The main absorption features are detected in the continuum of 15 out of our 20 galaxies, allowing us to measure several of the Lick indices (Worthey et al. 1994) and to compare them with the ones obtained for two samples of nearby quiescent galaxies: Kennicutt (1992ab; hereafter K92) for late-type galaxies and Trager et al. (1998; T98) for early-type

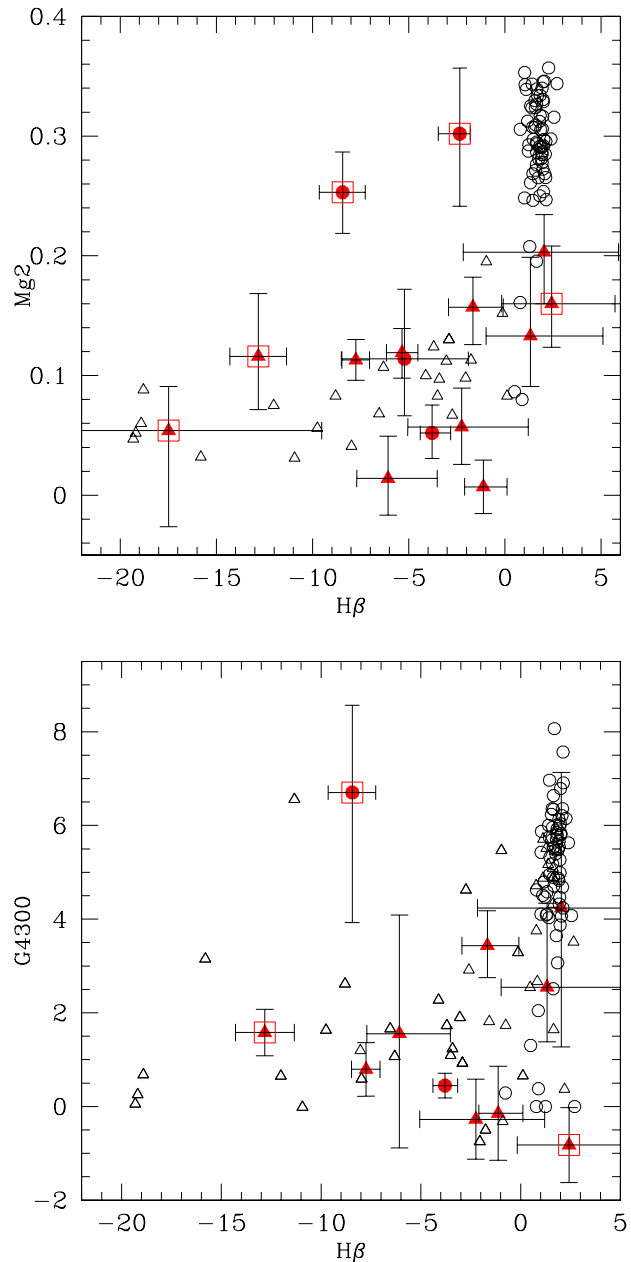


**Figure 6.** Comparison of the Lick indices measured in our quasar hosts (filled symbols) with two samples of non-active galaxies. Open squares identify the galaxies where the gas is found to be ionized by the central quasar (Section 7.2). The indices for the samples of Kennicutt (K92) and Trager (T98) are plotted as open symbols. For all three samples, circles indicate elliptical galaxies and triangles indicate other types of galaxies. The error bars are the combination of the uncertainties on the index measurements given the data dispersion and the uncertainties from deconvolution (see Section 4.1). Our quasar hosts compare well with the late-type galaxy sample, matching the subsample of Sc or later emission line galaxies.



**Table 4.** Summary of the main spectral characteristics for the 20 host galaxies. (1-) Object name, (2-E) presence of emission lines, (3-A) detection of absorption lines, (4 to 7) type of analysis performed on the spectrum: gas metallicity (met), star formation rate (sfr), extraction of a radial velocity curve (rvc), and mass modelling (mass). The ionization source of the gas (AGN or young stars) could be determined for all objects with emission lines, while Lick indices could be measured in all objects with absorption lines.

| Object name  | E | A | met | sfr | rvc | mass |
|--------------|---|---|-----|-----|-----|------|
| HE 0132–4313 | x | x | -   | -   | x   | x    |
| HE 0203–4221 | x | x | -   | -   | x   | -    |
| HE 0208–5318 | x | x | x   | x   | -   | -    |
| HE 0306–3301 | x | x | x   | x   | x   | -    |
| HE 0354–5500 | x | x | -   | -   | x   | -    |
| HE 0441–2826 | x | x | x   | x   | -   | -    |
| HE 0450–2958 | x | - | -   | -   | -   | -    |
| HE 0530–3755 | x | - | -   | -   | -   | -    |
| HE 0914–0031 | x | x | x   | x   | x   | x    |
| HE 0956–0720 | - | - | -   | -   | -   | -    |
| HE 1009–0702 | x | x | x   | x   | x   | x    |
| HE 1015–1618 | - | - | -   | -   | -   | -    |
| HE 1029–1401 | x | x | -   | -   | x   | -    |
| HE 1228+0131 | - | - | -   | -   | -   | -    |
| HE 1302–1017 | x | x | x   | x   | x   | -    |
| HE 1434–1600 | x | x | -   | -   | x   | -    |
| HE 1442–1139 | - | x | -   | -   | -   | -    |
| HE 1503+0228 | x | x | x   | x   | x   | x    |
| HE 2258–5524 | x | x | -   | -   | x   | -    |
| HE 2345–2906 | x | x | x   | x   | x   | x    |

galaxies. The  $\text{RED}_{\text{mE}}^1$  package was used to carry out the measurements (Cardiel 1999). We use the published indices of Trager’s sample, while we make our own measurements on the Kennicutt atlas of galactic spectra. As only few absorption features are detected in our spectra, estimates of the stellar velocity dispersions are not reliable. We therefore do not correct our measurements for the velocity dispersion. However, it should be pointed out that such a correction would remain within the error bars, and would not affect the global characterization of the sample.

The most prominent absorption lines detected in our spectra are the CaII H and K lines (3969 Å and 3933 Å), the MgII triplet around 5174 Å and the G-band of CH at 4303 Å. The latter is not detected in all galaxies. Hydrogen absorption lines, when present, are always blended with emission. In Fig. 6 the Lick indices Mg2 and G4300 are plotted versus the  $\text{H}\beta$  index (see Worthey et al. 1994 for a detailed definition of the indices). A negative index stands for emission. CaHK is not presented because it is not available in T98. The Mg2 index windows are modified with respect to the original definition, in order to avoid contamination from the [OIII]4959 Å emission line: we change the original continuum windows [4895.125–4957.625] and [5301.125–5366.125] Å to [4895.125–4947.625] and [5301.125–5356.125] Å.

In Fig. 6, the elliptical galaxies from Trager’s sample (open circles) all show large Mg2 and G4300 indices, indica-

tive of the high metallicities associated with old stellar population. They also show  $\text{H}\beta$  in absorption, representative of gas-poor galaxies. We restricted the Kennicutt sample (open triangles) to spiral galaxies showing emission lines, as almost all galaxies in our sample show prominent emission lines. The K92 spiral galaxies are located at lower metallicities than the T98 ellipticals and generally display negative  $\text{H}\beta$ , accounting for globally young stellar populations and an important ionized gas content.

Our QSO hosts (filled symbols) follow well the distribution of late-type galaxies, compatible with a subsample of normal Sc population or later because of their similar  $\text{H}\beta$  emission lines. The hosts of HE 0132-4313, HE 1442-1139, and HE 2258-5524, presenting faint or barely detectable  $\text{H}\beta$  emission lines, lie at the limit between the K92 and T98 samples. They likely host stellar populations characteristic of galaxy types between E and Sa. Among the galaxies identified as ellipticals from their morphology (filled circles; Bahcall et al. 1997; Kuhlbrodt 2003), only two hosts, HE 1029-1401 and HE 1434-1600, stand in a range of metallicities corresponding to ellipticals, but out of the distribution of the T98 comparison sample because of their important  $\text{H}\beta$  emission.

The ISM of some of our QSO hosts is found to be ionized by the central AGN itself (see Section 7.2). We represent these objects with an open square around the filled symbol in Fig. 6, as their location in the diagrams may be biased by a significant contribution of  $\text{H}\beta$  emission induced by the nuclear ionization. It is the case for the old population hosts, and probably for the two objects with extreme  $\text{H}\beta$  emission which, without this contribution, would rather be located in the bulk of the distribution.

Only two objects in our sample have stellar populations characteristic of genuine elliptical galaxies (see Table 3), and 3 have populations intermediate between E and Sa. The other 10 objects display stellar populations typical of young discs rather than bulge-dominated galaxies.

In the following, we classify the objects according to their host morphology. When the classification of an object is secure, we refer to it as Elliptical or Disc. Among the unclassified hosts, we indicate the galaxies with young stellar population (YP) with a distinctive symbol to distinguish them from the objects for which we have no secure information at all. In all but one object for which we have both morphological and stellar population characterization, the young stellar population of the host is associated to disc morphology.

## 7.2 Ionization source

Diagrams comparing the intensity ratios between different emission lines of the host galaxies allow to infer the source of the gas ionization in the ISM. Such diagrams (Baldwin et al. 1981; Veilleux & Osterbrock 1987) are often used to discriminate between Seyferts and star-forming galaxies, when only a global quasar-plus-host spectrum of the object is available. Here we construct these diagrams for the host spectra only, after the nuclear component has been removed. We therefore determine the main source of ionization of the gas across the galaxy, excluding the AGN itself. As far as possible, we choose flux ratios of lines with similar wavelengths, in order to minimize the impact of dust extinction. Our diagrams are

<sup>1</sup> <http://www.ucm.es/info/Astrof/software/reduceme/reduceme.html>

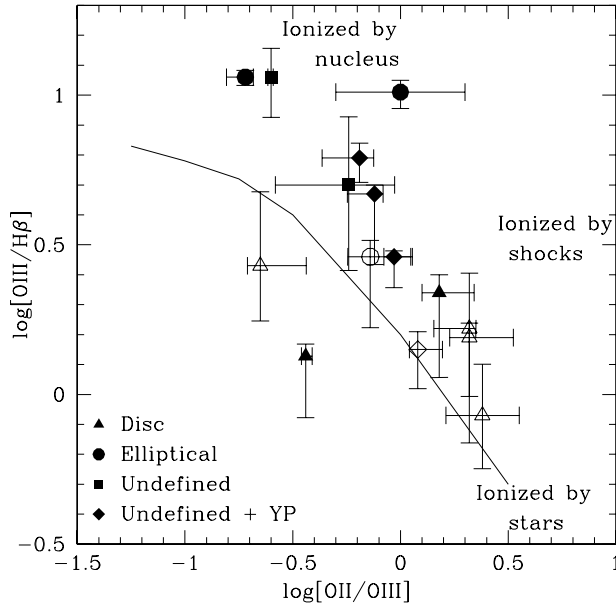


**Figure 7.** Example of diagnostic diagram constructed following Baldwin et al. (1981), for our sample of quasar hosts. Filled symbols are for hosts that display signs of interactions, while open symbols indicate isolated hosts. Error bars are a quadratic combination of errors on the measurement and on the deconvolution process (see Section 4.1). The solid line follows the locus of typical HII regions. Most of the interacting hosts are in the upper part of the diagram, where the central AGN is responsible for the gas ionization. A correction for reddening would shift the points horizontally towards the right, i.e. further away from the HII region locus.

constructed using the  $[\text{OIII}]/\text{H}\beta$ ,  $[\text{NII}]/\text{H}\alpha$  and  $[\text{SII}]/\text{H}\alpha$  line ratios, the latter two being sometimes less accurate because of the difficulty to separate the quasar and host components  $\text{H}\alpha$  region when it is overcrowded by atmospheric lines. Although it is more sensitive to reddening, the  $[\text{OII}]/[\text{OIII}]$  ratio is also used because it can be easily measured in the majority of our quasar hosts. Such diagrams are presented in Figs. 7 and 8, and the measured values are listed in Table 5.

Although reddening by dust cannot be corrected for exactly, its impact on the position of the points in Fig. 7 can be estimated. For that purpose, we selected the subsample of objects that have accurate quasar-host separation in the  $\text{H}\alpha$  region and we estimated their reddening from the Balmer decrement. Using a Whitford reddening curve (Miller & Mathews 1972), we then corrected the  $[\text{OII}]/[\text{OIII}]$  ratio. These reddening corrections range from 0.05 to 0.44. Applying them would result in shifting the points to the right by this amount in Fig. 7.

We find two major sources of ionization: the hard radiation field of the active nucleus itself (power-law ionization source) and ionization by the softer photons produced by young stars in HII regions. However, when a reddening correction is applied, most of the points in Fig. 7 move further away from the HII locus. Does this mean that none of our hosts is ionized by pure stellar emission? Indeed, most of the low ionization objects (low  $[\text{OIII}]/\text{H}\beta$  ratio) move, when reddening is taken into account, into the region which, according to Baldwin et al. (1981), corresponds to shock-heated

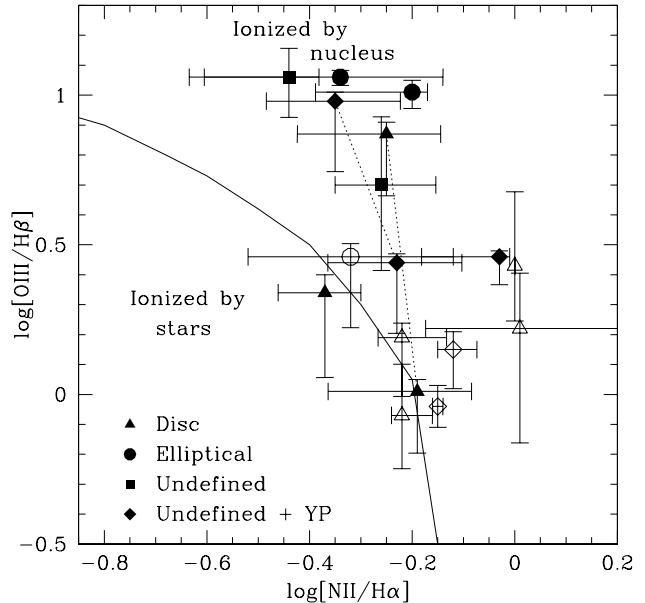


**Figure 8.** Diagnostic diagram similar to Fig. 7 but for the  $[\text{NII}]/\text{H}\alpha$  ratio. In this case, the solid line is the separation between ionization of the gas by stars (lower left) and by the central quasar (upper right). Filled symbols are for hosts which display signs of interactions, while open symbols indicate isolated hosts. Some of the galaxies in our sample are not shown because of unreliable spectral separation between NII and  $\text{H}\alpha$ . The symbols connected by dotted lines correspond to the same hosts, in which different regions display different ionization levels (see Table 5).

gas. The objects further away from the HII region locus after reddening correction (i.e. those with highest reddening) are also galaxies undergoing a minor merger, in which a small companion is being captured by the host. Those small encounters can possibly create shocks, which produce an additional source of ionization, above the young stars themselves.

Table 5 gives the intensity ratios integrated over the whole galaxy (without nucleus) and the corresponding classification of the main ionization source, either hot stars (H), the AGN (A) or shocks (S). The availability of 2D spectra allows, for objects with the largest spatial extension and sufficient S/N in the emission lines, to measure the intensity ratios in different parts of the galaxy. The three objects in the second part of Table 5 are those in which the diagnostic varies significantly with distance from the centre. It is striking that, for all three objects, while the centre region shows predominantly HII regions ratios (or intermediate ones), the ionization of the outer parts is clearly dominated by the AGN radiation field. While it may not necessarily mean that the AGN ionization power is larger at large distances, it suggests that the range of AGN ionization is larger than the range of star formation (and hence of HII regions). The latter appears more concentrated towards the centre, while the quasar radiation field reaches larger distances. Note that these three hosts are involved in gravitational interactions (see Section 8).

All but one of the elliptical host galaxies harbour gas and tend to present high ionization levels, i.e., have ISM ion-

**Table 5.** Logarithmic line ratios for the host galaxies with emission lines. The last column gives our diagnostic on the main ionization source: H stands for normal HII regions, S for shock heated gas, A for ionization by the active nucleus. I stands for *intermediate* between A and H, and consists of a mixture of different ionization sources. Oxygen line ratios indicated in parenthesis are corrected for reddening. The ratios involving the  $H\alpha$  line for HE 0441-2826 are only indicative, as the correction for atmospheric absorption is poor for this object (see Fig. 19). The second part of the table lists the three objects for which the ionization source is found to vary significantly with distance from the nucleus. In those cases, the first line corresponds to the integrated spectrum, the second to the central regions of the host and the third to the external ones.

| Object               | $\frac{OII}{OIII}$ | $\frac{OIII}{H\beta}$ | $\frac{NII}{H\alpha}$ | $\frac{SII}{H\alpha}$ | I.S. |
|----------------------|--------------------|-----------------------|-----------------------|-----------------------|------|
| HE 0132–4313         | -                  | -0.04                 | -0.15                 | -                     | H    |
| HE 0208–5318         | 0.08               | 0.15                  | -0.12                 | -                     | H    |
| HE 0306–3301         | 0.18 (0.62)        | 0.34                  | -0.37                 | -0.63                 | H/S  |
| HE 0441–2826         | -0.14              | 0.46                  | (-0.32)               | (-0.69)               | H    |
| HE 0914–0031         | -0.65              | 0.43                  | -                     | -                     | H    |
| HE 1009–0702         | 0.32 (0.44)        | 0.22                  | 0.01                  | -0.28                 | H/S  |
| HE 1302–1017         | -0.03              | 0.46                  | -0.03                 | -0.39                 | H/S  |
| HE 1503+0228         | 0.32 (0.43)        | 0.19                  | -0.22                 | -                     | H/S  |
| HE 2345–2906         | 0.38 (0.44)        | -0.07                 | -0.22                 | -0.32                 | H    |
| HE 0530–3755         | -0.24              | 0.70                  | -0.26                 | -                     | I    |
| HE 0450–2958         | -0.60              | 1.06                  | -0.44                 | -0.28                 | A    |
| HE 1029–1401         | 0.02 (0.39)        | 1.01                  | -0.20                 | -0.02                 | A    |
| HE 1434–1600         | -0.72              | 1.06                  | -0.34                 | -0.65                 | A    |
| HE 0203–4221         | -0.19              | 0.79                  | -                     | -                     | I    |
| <i>centre</i>        | -0.16              | 0.72                  | -                     | -                     | I    |
| <i>2.5 to 12 kpc</i> | -0.26              | 0.92                  | -                     | -                     | A    |
| HE 0354–5500         | -0.44              | 0.13                  | -0.20                 | -0.45                 | H    |
| <i>centre</i>        | -0.41              | 0.01                  | -0.19                 | -0.39                 | H    |
| <i>9 to 20 kpc</i>   | -0.65              | 0.87                  | -0.25                 | -                     | A    |
| HE 2258–5524         | -0.12 (0.21)       | 0.67                  | -0.22                 | -0.55                 | I    |
| <i>centre</i>        | -0.07              | 0.44                  | -0.23                 | -0.50                 | H    |
| <i>3 to 8 kpc</i>    | -0.24              | 0.98                  | -0.35                 | -0.75                 | A    |

ized by the quasar. Even though our sample contains only 4 elliptical galaxies, there might be a connection between this tendency and the fact that elliptical hosts exhibit bluer colours than quiescent elliptical (e.g., Jahnke et al. 2004). This blue colour excess is often explained by the presence of a young stellar population, but since the ellipticals in our sample show large amounts of ionized gas and globally old stellar population, we investigate if the strong gas emission lines can account for the observed bluer colours. We therefore estimate the restframe  $B - V$  colours of our elliptical hosts directly on the integrated spectra, in two ways: 1- using the 1D spectrum of the host, and 2- using a modified version of the spectrum where the emission lines have been removed. We find that the emission lines can account for a colour variation of about 0.03 mag. As the average colour difference between active and quiescent ellipticals is as large as  $\Delta(B-V) = 0.44$  (Jahnke et al. 2004), we can conclude that the presence of ionized gas is not sufficient to explain the bluer colours of active galaxies compared to quiescent ones.

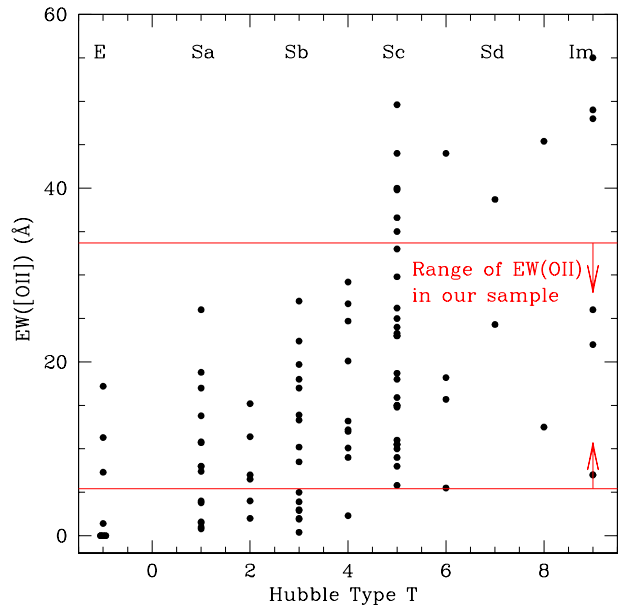


**Figure 9.** EW([OII]) as a tracer of star formation rate, in the samples of galaxies from Kennicutt (1992ab) and from Jansen et al. (2000) restricted to the brightest part of the luminosity function. The range of EWs spanned by our HII galaxies is shown by the horizontal lines, suggesting that there are no quasar hosts with low star formation rate, nor extreme starbursts. The majority of quiescent elliptical galaxies presents no [OII] emission line at all while most of our elliptical hosts do (not included in this HII region-like subsample).

### 7.3 Star formation rate

Star formation rates can be estimated only for galaxies presenting line ratios characteristic of HII regions, thus avoiding extra emission arising from nuclear ionization. We therefore restrict this section to the objects labelled *H* in Table 5, excluding HE 0132-4313 in which [OII] is not detected. From the discussion of Section 7.1, we note that all galaxies in this subsample present a young stellar population. Five of them are spirals, one is elliptical and the last two have undefined morphologies.

Several estimators of the star formation rate (SFR) are available in the optical range, one of the most widely used being the integrated flux in the  $H\alpha$  emission line. However, because of the poor quasar-host separation at this wavelength for several objects, we adopt another indicator, [OII] 3727 Å, as suggested by Kennicutt (1998) and Kewley et al. (2004). In order to get rid of the effect of dust extinction, we rely on EWs rather than fluxes and, thus, directly compare our EW([OII]) with measurements in non-active galaxies, sorted by Hubble type. As a reference sample, we use the atlas of galaxies from Kennicutt (1992ab) augmented by the sample of nearby galaxies of Jansen et al. (2000). We restrict ourselves to the brightest part of the luminosity function with  $M_B < -18$ , as EW([OII]) is slightly correlated with magnitude.

Figure 9 shows the measurements, with a slight evolution of EW([OII]) with Hubble type, later-type galaxies displaying larger EWs. We overplot on the reference sample the range of values spanned by our quasar hosts. Figure 9

shows that while none of our hosts displays a low SFR, none of them has very large one, as could be found in starburst galaxies. The EW([OII]) of our sample are compatible with a population of regular disc-dominated galaxies, as the stellar population analysis also suggests.

Note that, for all but one host, the extreme values of over- or undersubtraction of the quasar spectrum, derived from the method explained in Section 4.1, do not move the values outside of the EW range shown in Figure 9, thus leading to the same conclusions. Only HE 1302-1017, at the limit of oversubtraction of the nuclear component, would present an EW compatible with extreme starburst.

#### 7.4 Gas metallicity

The oxygen abundance in the ISM, as an indicator of the enrichment of gas by stars in the galaxies, allows to further characterize our subsample of QSO hosts in which stars constitute the main gas ionization source. We first describe the methods used to evaluate the gas metallicity, then we compare our sample to non-active galaxies.

The standard measurement of the gas metallicity,  $\log(\text{O}/\text{H})+12$ , can be evaluated by the parameters R23 (ratio of collisionally excited emission-line intensities) and O32 (indicator of ionization parameter):

$$R23 = \frac{I([\text{OII}]3727 \text{ \AA}) + I([\text{OIII}]4959 \text{ \AA} + 5007 \text{ \AA})}{I(\text{H}\beta)}$$

$$O32 = \frac{I([\text{OIII}]4959 \text{ \AA} + 5007 \text{ \AA})}{I([\text{OII}]3727 \text{ \AA})}$$

The R23-oxygen abundance relation is globally double-valued (see e.g. McGaugh 1991). For a given value of O32, the parameter R23 corresponds to two metallicities, one for metal-rich gas (on the so-called *upper branch*) and one for metal-poor gas (*lower branch*). Gas with  $\log(\text{O}/\text{H})+12 > 8.5$  is considered metal-rich, while with  $\log(\text{O}/\text{H})+12 < 8.3$  it is metal-poor. In the metal-rich regime, R23 decreases progressively with increasing metallicity, since higher metal abundance implies a more efficient cooling and thus a lower degree of collisional excitation. Below the turnaround region around  $\log(\text{O}/\text{H})+12 = 8.4$ , the oxygen abundance becomes the dominant factor and the R23 parameter decreases with decreasing metallicity. This R23 degeneracy is broken by the analysis of the ratios NII/OII or NII/H $\alpha$ , which both grow linearly with metallicity, distinguishing between high and low metallicity regimes. We use here the calibrations for upper and lower branches from McGaugh (1991), as given in Eqs. 7 to 10 of Kobulnicky et al. (1999).

While these estimators have been widely used to infer oxygen abundances in well resolved local HII regions, Kobulnicky et al. (1999) have shown that global emission-line spectra could also indicate the chemical properties of distant star forming galaxies. A reliable estimate of the metallicity can also be reached with EWR23 and EWO32, the same parameters as R23 and O32 but computed on EWs rather than on intensities (Kobulnicky et al. 2003). As the line EWs are insensitive to interstellar reddening effects, the EW version is to be preferred in our case since extinction cannot be properly corrected for the whole sample. The EWR23 method is however affected by an additional un-

**Table 6.** Gas metallicities expressed as  $\log(\text{O}/\text{H}) + 12$ , computed from McGaugh (1991) EWR23 correlation as given in Kobulnicky et al. (1999). We corrected the H $\beta$  EWs of the last two objects for underlying stellar absorption. The maximum bulge-to-host ratio is estimated as discussed in the text.

| Object name  | $\log(\text{O}/\text{H})+12$ | $1\sigma$ error | bulge/host |
|--------------|------------------------------|-----------------|------------|
| HE 0208–5318 | 8.41                         | 0.11            | 0.8        |
| HE 0306–3301 | 8.45                         | 0.16            | 0.5        |
| HE 0441–2826 | 8.28                         | 0.12            | -          |
| HE 0914–0031 | 8.83                         | 0.11            | 0.7        |
| HE 1009–0702 | 8.34                         | 0.14            | 0.2        |
| HE 1302–1017 | 8.48                         | 0.08            | 0.8        |
| HE 1503+0228 | 8.53                         | 0.05            | 0.3        |
| HE 2345–2906 | 8.79                         | 0.05            | 0.4        |

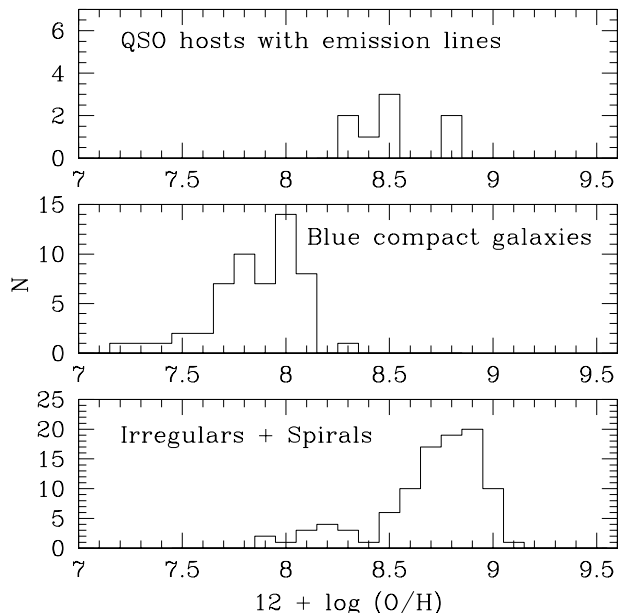


**Figure 10.** Histogram of gas metallicities estimated on global spectra in our sample (top panel), in blue compact galaxies (Izotov 1999, middle panel), irregulars and spirals (Kewley et al. 2005, bottom panel). While two galaxies lie perfectly in the spiral distribution, the other hosts present intermediate metallicities, in between blue compact and spiral galaxies.

certainty of around 0.1 dex in comparison to other methods (Moustakas & Kennicutt 2005).

The oxygen abundances in our sample deduced from this EW calibration are listed in Table 6. Most of these abundances correspond to the turnaround region, with NII/OII and NII/H $\alpha$  ratios pointing to the metal-rich branch. HE 0441–2826, the most metal-poor object of the sample, is at the extreme limit of validity of the upper branch.

We compare in Fig. 10 the oxygen abundances of QSO host galaxies presenting gas ionized by stars to other samples of integrated spectra for emission-line galaxies: a sample of blue compact galaxies, representing very metal-deficient environments (Izotov 1999), and the sample of nearby irregulars and spirals of Jansen et al. (2000), used in the previous section for SFR characterization, with metallicities

computed by Kewley et al. (2005). This sample contains all types of spirals, from S0 to Sd. The earlier-type spirals (S0-Sab) tend to contain gas with higher metallicity, with  $\log(\text{O}/\text{H})+12$  around 9, while the small bump at lower metallicities (between 8 and 8.5) in this distribution roughly corresponds to irregular galaxies.

The two most metal-rich galaxies of our sample, HE 2345-2906 and HE 0914-0031, sit in the middle of the spiral distribution. As for both we find disc morphologies with no trace of interaction and medium to low SFR, we suggest that they have undergone a normal spiral galaxy evolution. In the case of HE 0914-0031, the cause of ignition of the quasar is thus still unknown. Recent *HST*/ACS images of HE 2345-2906, currently under analysis (Letawe et al., in prep.), reveal a prominent bar which could be an efficient driver of gas and dust to the central region, thus triggering the QSO activity, as suggested by Crenshaw et al. (2003) for another type of AGNs, the Narrow Line Seyferts 1 (NLS1).

The rest of the sample has metallicities in between the blue compacts and the more evolved spirals. The gas in these host galaxies is similar to the gas of irregulars, thus suggesting a rather inefficient star formation. HE 1302-1017, with the highest SFR of the sample, an irregular radial velocity profile and signs of small companions merging in, might constitute a very young system where both nuclear activity and star formation have just been triggered by the mergers. For HE 0306-3301, the minor merger only induced nuclear activity without enhancing drastically the star formation. The four other galaxies show no trace of gravitational interaction. They must also be young systems (compatible with their young stellar population, and with the disc morphology found for most of them) but in which the origin of activity remains, as for HE 0914-0031, still unexplained. It is only at the limit of undersubtraction of the quasar light that the metallicities would become compatible with normal spirals, the oversubtraction still diminishing the host metallicities towards values typical of irregular galaxies.

The cosmological evolution of the comparison samples from  $z \sim 0.3$  to  $z = 0$  has not been taken into account in the histogram. However, following PEGASE2 chemical evolution models as presented in Maier et al. (2006), this cosmological evolution on a standard metallicity-luminosity diagram does not exceed 0.1 dex in metallicity and 0.5 dex in magnitude, as shown in Fig. 11. The aforementioned conclusions on galactic histories are thus not significantly affected by a correction for evolution, as Fig. 11 shows that evolutionary effects are not large enough to explain the low metallicities observed at a given host luminosity.

Following the  $M_{\text{BH}} - M_{\text{bulge}}$  scaling relation observed in active and inactive galaxies (McLure & Dunlop 2002), the observed luminosities of the quasars and thus their central masses ( $> 6 \cdot 10^7 M_{\odot}$ ) imply a substantial bulge ( $M_V < -21.3$ ) for all those host galaxies. The young stellar and gaseous content inferred for them do not match a bulge population, but rather a disc-like one. We estimate the bulge/host ratios from the  $V$  magnitudes of Table 1 and the bulge magnitudes from the  $M_{\text{BH}}$  estimates of section 9.2 (Table 6). Given that these ratios are upper limits because the host magnitudes are not corrected for reddening and may be underestimated (section 3.2), they are fully consistent with typical late-type spirals.

In the majority of the cases analysed in this section, the

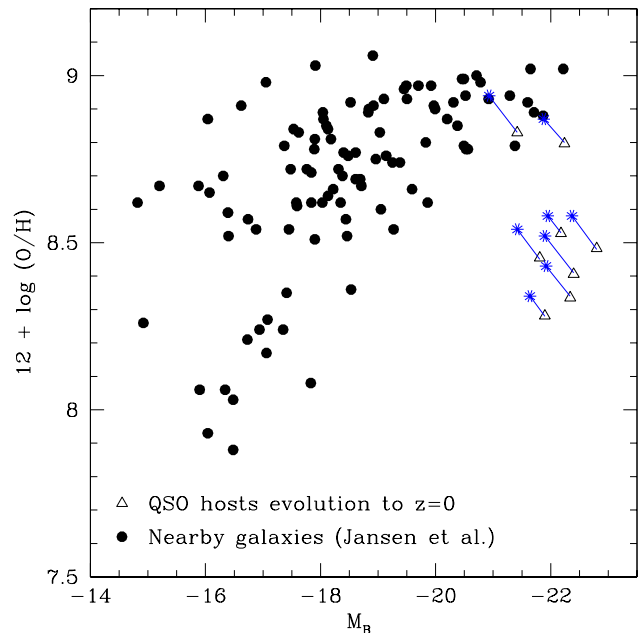


**Figure 11.** Metallicity-Luminosity diagram. The Jansen sample of nearby galaxies is presented with solid circles, whereas our sample and its expected evolution is shown from the observed redshift (open triangle) to  $z = 0$  (star-like symbols).

quasar activity obviously appears in galaxies in which the star formation has had a low efficiency so far. This observation could be linked to a selection effect, the most metal-rich galaxies being more likely to contain more dust and thus suffer from extinction, falling below the magnitude criterion of our sample selection. But this also suggests that these spiral hosts are at an early stage of their evolution and, thus, that one of the mechanisms for triggering quasar activity may be linked to the formation or very early evolution of (at least some) spiral galaxies. As discussed in the next section, galactic collisions are obviously another (and more powerful) triggering mechanism.

The origin of the triggering of QSO activity in the young spirals discussed in the present section might be confined to the central part ( $< 1$  kpc, i.e. the pixel size of our data) of the galaxy. In such a case, it would not be detected from a study of the global host characteristics analysed here.

## 7.5 Average spectra

For the sake of illustration, we computed average spectra for several subsamples of our 20 host galaxies. The averages are presented in Fig. 12 for galaxies classified as spirals and for galaxies with an undefined type and a young stellar population. Fig. 13 shows average spectra for galaxies with an ISM ionized by the central quasar on one hand and by stars on the other hand. The four spectra with the lowest S/N have been removed from the averages, as well as HE 0450-2958 for which no stellar continuum is detected at all. The averaging is performed on the spectra in the rest-frame. They are all normalized to unit flux at  $5100 \text{ \AA}$  and weighted according to their S/N. The two average spectra in Fig. 12 present similar global features, indicating that an important fraction of the galaxies with an undefined morphological type

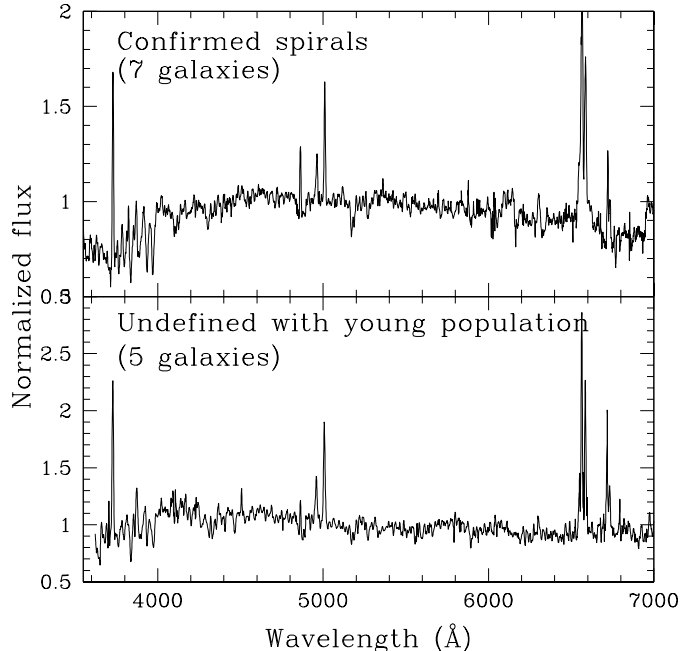


**Figure 12.** *Top:* average spectrum for spiral hosts. *Bottom:* average spectrum for hosts with an undefined morphology but young stellar population.

could be disc-dominated. In Fig. 13, the average on galaxies with gas ionized by stars has a blue continuum with prominent Balmer absorption lines while the continuum for galaxies where the gas is ionized by the nucleus is flatter. As expected in HII regions, the blue slope and strong Balmer lines indicate young stars, while ionization by the quasar appears in a mix of galactic types with a larger range of slopes, hence producing on average a flatter continuum.

## 8 DYNAMICS AND INTERACTION

### 8.1 Radial velocity curves and mass modelling

We take advantage of the very different spectral widths of the emission lines in the quasar and in the host galaxy to carry out an accurate quasar-host separation in the emission lines. This procedure, described in detail in Courbin et al. (2002), allows to extract detailed information on the velocity of the gas in the host galaxy.

This spectral decomposition method is applied to all the spectra showing sufficiently high signal-to-noise ( $S/N > 5$  per pixel) in the external parts of the hosts. Figure 14 presents the extracted radial velocity curves. When several emission lines are extracted for the same object, they are represented by different symbols on the same plot. Figure 14 shows that many radial velocity curves are distorted and thus cannot be fitted by simple mass models as described in Courbin et al. (2002). These galaxies are probably disturbed by ongoing or past gravitational interactions with nearby companions.

Fitting a mass model to the velocity curves requires knowledge of the inclination and position angle (PA) of the disc (if any is involved). They are estimated using the acqui-

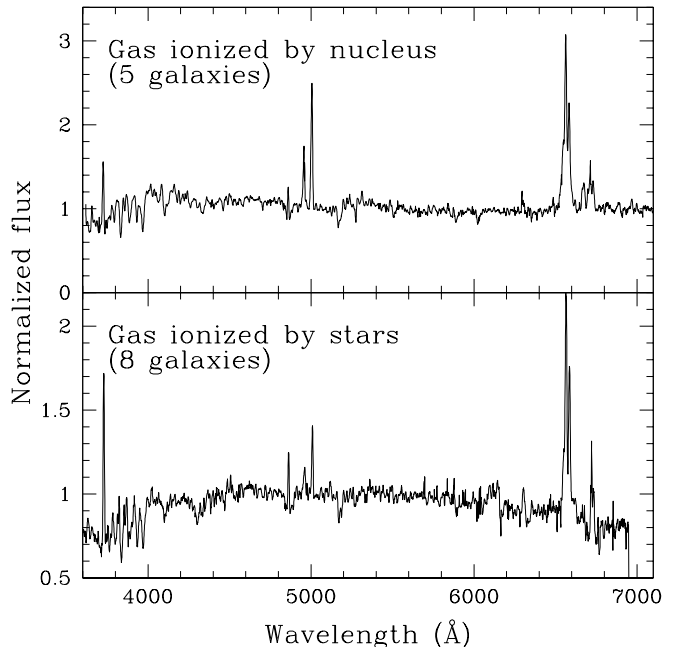


**Figure 13.** *Top:* average spectrum for quasar hosts where the gas is ionized by the nucleus. *Bottom:* average spectrum for hosts where the gas is ionized by stars.

sition images obtained before each spectrum, using a modified version of the MCS deconvolution algorithm that includes a 2D analytical model for the host galaxy.

The results of the mass model fits on symmetrical velocity curves (see Courbin et al. 2002) are represented by a solid line in Fig. 14. The corresponding mass estimates are given in Table 7, along with the inclination of the disc component on the line of sight and the angle of the major axis relative to the slit. The mass model includes a dark matter halo, a rotating stellar disc, and a fixed central mass (from Section 9.2). With our spatial resolution (0.2 arcsec per pixel, which translates into a linear scale between 0.6 and 1.0 kpc depending on redshift), adding a bulge component does not improve the fits and prior knowledge of the central mass (e.g., estimates using the  $H\beta$  line of the quasar) do not constrain the model significantly. The mass modelling does not allow to weight the relative contributions of disc and bulge in the galaxies. Table 7 shows that these hosts are rather massive spirals, while not disproportionate relative to their inactive counterparts.

Although the velocity curves of HE 1434-1600 and HE 1029-1401 look symmetrical, they cannot be fitted with a realistic set of parameters. Close scrutiny of the images reveals, in both cases, elliptical galaxies with neighbours merging in or interacting, which excludes the assumption of a simple circular motion. The special case of HE 1434-1600 has been presented in Letawe et al. (2004). HE 1029-1401 is seen nearly face-on (Kuhlbrodt 2003), and interpreting radial velocities as rotational velocities would give unrealistic masses (up to  $10^{17} M_{\odot}$ ) given the inclination angle.

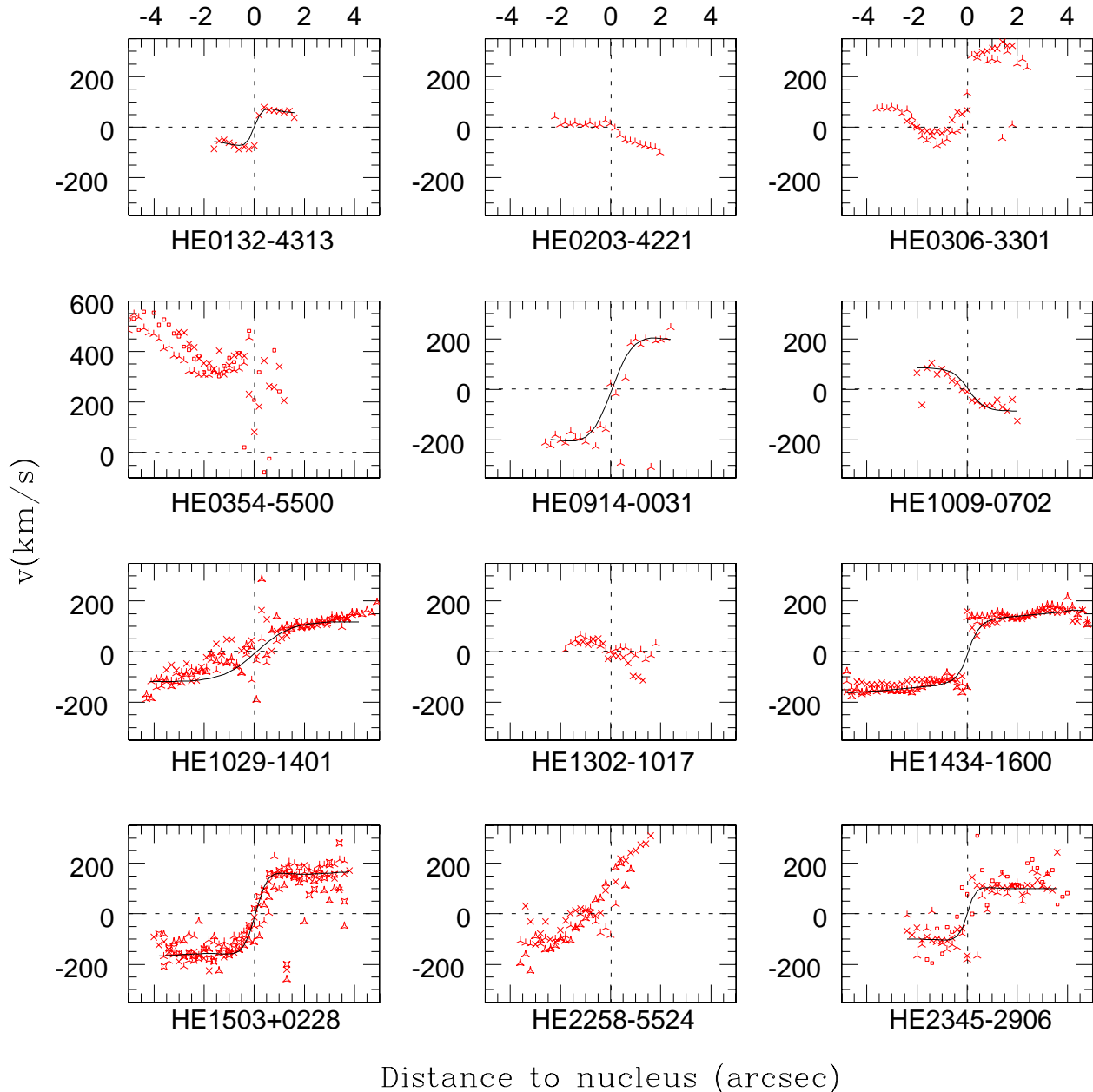


**Figure 14.** Extracted radial velocity curves for all objects with sufficient S/N in the emission lines. The  $H\alpha$  line is represented by 4-arms crosses. Since some grisms have overlapping spectral ranges the  $H\alpha$  line may appear twice. In such a case, the measurement of this line in the second grism is plotted as 4-arms stars. The [OIII] line is represented by 3-arms crosses (and stars when a second measurement is available) and the [OII] line is represented by squares. The solid lines represent mass model fits when relevant (see text).

## 8.2 Interactions

Signs of interaction are found for nine out of the twenty galaxies in our sample, i.e., in 2 spirals, 2 ellipticals and in 5 galaxies with undefined morphology. The hosts whose images (from this or previous studies) show irregular shapes, reminiscent of interaction are labelled “interac” in Fig. 5, while a classification of the signs of interactions is given in Table 1: close companion outside the galaxy (1), tidal tails (2) or merger, i.e. companion inside the galaxy (3). A confirmation of those perturbations is provided by the extracted

radial velocity curves presented in Fig. 14. All the hosts with asymmetric curves also have images with irregular shapes. We thus find that  $\sim 50$  per cent of our host galaxies display signs of interaction, which is compatible with several previous studies (Smith et al. 1986; Hutchings & Neff 1992; Bahcall et al. 1997; Sanchez et al. 2004; Jahnke et al. 2004). This is also compatible with the fraction of interacting but non-active galaxies according to Dunlop et al. (2003).

The diagnostic diagram in Fig. 8 shows that *every galaxy with long-range ionization by the nucleus is also inter-*

**Table 7.** Mass estimates for spiral galaxies with symmetrical rotation curve. The adopted model consists of a rotating disc, a dark matter halo and a central mass. All masses are in solar units.  $i$  is the inclination of the disc and  $\phi$  is the angle of the major axis of the galaxy relative to the slit. The determination of these angles is the main source of uncertainty in our mass estimates. The last two galaxies have smaller error bars because *HST* images are available to determine  $i$  and  $\phi$ .

| Object       | $\phi$<br>( $^{\circ}$ ) | $i$<br>( $^{\circ}$ ) | $\log M$<br>( $r < 10\text{kpc}$ ) |
|--------------|--------------------------|-----------------------|------------------------------------|
| HE 0132–4313 | 78                       | 37                    | $11.9^{+0.2}_{-0.7}$               |
| HE 0914–0031 | 68                       | 32                    | $12.6^{+0.5}_{-0.3}$               |
| HE 1009–0702 | 66                       | 29                    | $11.7^{+0.5}_{-0.3}$               |
| HE 1503+0228 | 18                       | 46                    | $11.0^{+0.1}_{-0.1}$               |
| HE 2345–2906 | 70                       | 36                    | $12.0^{+0.1}_{-0.1}$               |

*acting.* The mechanism at work is probably similar to the one responsible for the Extended Emission Line Regions (EELR) usually associated with radio-loud quasars (Boroson et al. 1985; Stockton & McKenty 1987) or Seyferts with radio emission (Evans et al. 1999), as presented in Stockton et al. (2002). During the interaction, the dust surrounding the quasar is swept out or sufficiently perturbed, letting the ionizing nuclear beam reach the gas in the outer parts of the galaxy and ionizing it. Shocks induced by the interaction are considered as complementary sources of ionization. If the radio jet alone was sufficient to produce EELR, this phenomenon would be more common in Radio Loud Quasars. The present study widens the type of galaxies where this phenomenon appears to the hosts of radio quiet quasars (RQQ), as only 2 out of the 7 cases of ionization by the central quasar display radio emission, at a level under the limit of classification as Radio Loud. To our knowledge, almost no high level ionization in galactic gas was previously found in RQQ (only one object in Stockton & McKenty 1987) probably only because of the lack of a detailed spectral study of this kind of host galaxies.

The unused slits of MOS spectrograph were placed on galaxies in the field, looking for companions at the same redshift as the quasar. While this is far from being an exhaustive analysis of the neighbourhood of each object, we find that 13 out of the 20 quasars have no detected neighbour, 4 quasars have one neighbour, 2 quasars have two and HE 1434-1600 has 5 neighbouring galaxies with close redshifts (Letawe et al. 2004).

## 9 NUCLEAR PROPERTIES

In this Section, we derive several properties of the quasars from their spectra and investigate their relation with host type, properties or environment. As the amount of dust on the line of sight to the quasar cannot be estimate with precision for each quasar, no correction for reddening is applied.

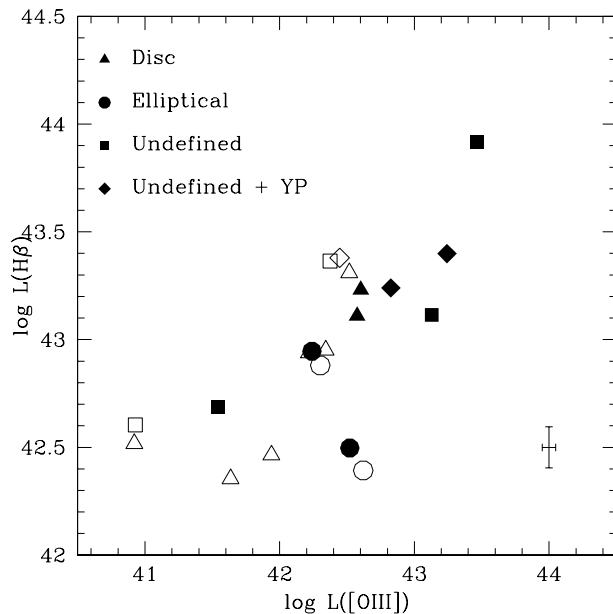


**Figure 15.** Luminosity of the nuclear  $H\beta$  versus luminosity of the nuclear  $[OIII]$  5007 Å emission line. The characteristics of the host galaxies are as stated in the legend. Filled symbols are for quasars hosted by galaxies that display signs of interaction. Typical  $1-\sigma$  error bars are shown, including errors on continuum subtraction for measurement of luminosities. Luminosities are in  $\text{erg s}^{-1}$ .

### 9.1 Spectral characteristics

The quasar properties are listed below and summarized in Table 8:

- The luminosities of emission lines:  $[OII]$  3727 Å and  $[OIII]$  5007 Å, indicators of the amount of gas and ionization of the Narrow Line Region (NLR) as well as  $H\beta$  for the Broad Line Region (BLR);
- The power law index  $\alpha$  of the continuum ( $F(\lambda) \propto \lambda^\alpha$ ), indicator of the power of the source. We evaluate it from the continuum slope in the  $\log F$  versus  $\log \lambda$  diagram between 4000 and 8000 Å;
- The monochromatic luminosity at 5100 Å, another indicator of the power of the nucleus, used for estimating the bolometric luminosity;
- The Balmer decrement  $H\alpha/H\beta$ . The Balmer decrement is dependent not only from extinction but also on physical density parameters in the BLR. It can however indicate the presence of dust.
  - The ratio  $[OIII]/H\beta$ ;
  - The FWHM of  $H\beta$ , useful for black hole mass determination (see Section 9.2);
  - The presence of FeII lines, noticeable by emission line multiplets, such as for instance in HE 0132-4313 but not in HE 0203-4221 (see Fig. 19).

Some of these spectral characteristics are plotted in Fig. 15, which shows that the quasars involved in galactic interactions (filled symbols) tend to have more emission from the gas in their immediate surroundings (higher luminosities in broad and narrow lines). As  $[OIII]$  is a good tracer of AGN power (Kauffmann et al. 2003), we conclude that



**Table 8.** Nuclear spectral characteristics for the whole sample and derived values of the BH mass and accretion rate. Luminosities are in  $\text{erg s}^{-1}$ ,  $\alpha$  is the power law index of the continuum ( $F(\lambda) \propto \lambda^\alpha$ ), and the FWHM of the broad  $\text{H}\beta$  component is expressed in  $\text{km s}^{-1}$ . Black hole masses are given in logarithm of solar masses and accretion rates in solar masses per year. The atmospheric absorption overlapping  $\text{H}\alpha$  in HE 0441-2826 spectrum was corrected before Balmer decrement evaluation.

| Object       | $\log L_{[\text{OII}]}$ | $\log L_{[\text{OIII}]}$ | $\log L_{\text{H}\beta}$ | $\alpha$ | $\log \lambda_{L51}$ | FeII | FWHM( $\text{H}\beta$ ) | $\frac{\text{H}\alpha}{\text{H}\beta}$ | $\frac{[\text{OIII}]}{\text{H}\beta}$ | $\log M_{\text{BH}}$ | $\dot{M}$ |
|--------------|-------------------------|--------------------------|--------------------------|----------|----------------------|------|-------------------------|--|---------------------------------------|----------------------|-----------|
| HE 0132–4313 | 41.24                   | 40.93                    | 42.60                    | -2.4     | 44.91                | x    | 1056                    | 3.2                                    | 0.02                                  | 7.21                 | 0.85      |
| HE 0203–4221 | 41.85                   | 43.24                    | 43.39                    | -2.1     | 45.33                |      | 7153                    | 7.4                                    | 0.63                                  | 9.15                 | 2.16      |
| HE 0208–5318 | 41.41                   | 42.44                    | 43.38                    | -2.5     | 45.07                |      | 6075                    | 3.0                                    | 0.11                                  | 8.83                 | 1.17      |
| HE 0306–3301 | 41.56                   | 42.57                    | 43.11                    | -2.3     | 44.98                | x    | 2346                    | 3.2                                    | 0.29                                  | 7.96                 | 1.01      |
| HE 0354–5500 | 41.66                   | 42.60                    | 43.23                    | -2.3     | 44.89                | x    | 2264                    | 3.4                                    | 0.09                                  | 7.86                 | 0.81      |
| HE 0441–2826 | 41.53                   | 42.62                    | 42.39                    | -2.2     | 44.99                |      | 5771                    | 5.3                                    | 1.69                                  | 8.87                 | 1.12      |
| HE 0450–2958 | 42.75                   | 43.46                    | 43.92                    | -2.3     | 45.58                | x    | 1282                    | 3.8                                    | 0.34                                  | 7.63                 | 1.96      |
| HE 0530–3755 | 41.80                   | 43.13                    | 43.11                    | -2.5     | 44.73                |      | 1721                    | 5.6                                    | 0.95                                  | 7.50                 | 0.54      |
| HE 0914–0031 | 40.89                   | 42.34                    | 42.95                    | -2.0     | 44.62                |      | 3072                    | 4.3                                    | 0.24                                  | 7.92                 | 0.42      |
| HE 0956–0720 | -                       | 42.37                    | 43.36                    | -2.2     | 45.03                |      | 2636                    | 3.7                                    | 0.1                                   | 8.07                 | 1.06      |
| HE 1009–0702 | 40.97                   | 42.22                    | 42.94                    | -1.6     | 44.71                | x    | 1826                    | 4.2                                    | 0.18                                  | 7.55                 | 0.54      |
| HE 1015–1618 | 41.08                   | 42.52                    | 43.31                    | -1.4     | 44.98                | x    | 2212                    | 3.1                                    | 0.17                                  | 7.89                 | 0.98      |
| HE 1029–1401 | 41.10                   | 42.24                    | 42.95                    | -1.3     | 44.69                |      | 5887                    | 4.1                                    | 0.19                                  | 8.60                 | 0.61      |
| HE 1228+0131 | -                       | 42.30                    | 42.88                    | -1.9     | 44.80                | x    | 1403                    | 3.8                                    | 0.26                                  | 7.41                 | 0.73      |
| HE 1302–1017 | 41.35                   | 42.83                    | 43.24                    | -2.0     | 45.33                |      | 2945                    | 4.7                                    | 0.36                                  | 8.38                 | 2.16      |
| HE 1434–1600 | 41.10                   | 42.52                    | 42.50                    | -1.4     | 44.19                |      | 7068                    | 7.4                                    | 0.95                                  | 8.37                 | 0.17      |
| HE 1442–1139 | 40.83                   | 40.92                    | 42.52                    | -1.7     | 44.30                | x    | 2063                    | 3.9                                    | 0.02                                  | 7.36                 | 0.21      |
| HE 1503+0228 | 40.14                   | 41.64                    | 42.35                    | -1.9     | 44.23                |      | 2990                    | 4.4                                    | 0.17                                  | 7.65                 | 0.19      |
| HE 2258–5524 | 40.93                   | 41.54                    | 42.69                    | -2.6     | 44.79                | x    | 1352                    | 3.4                                    | 0.07                                  | 7.31                 | 0.59      |
| HE 2345–2906 | 40.98                   | 41.94                    | 42.46                    | -2.0     | 44.15                |      | 4138                    | 4.0                                    | 0.29                                  | 7.87                 | 0.15      |

the quasars in interacting systems are also generally more powerful. This gives us direct evidence that the gravitational interactions constitute an essential process in bringing gas in the vicinity of the black hole and feeding it. Moreover, as we have seen from Fig. 8, highly ionized galactic gas is found in interacting systems, i.e. the ones which harbour the most powerful quasars. A high power of the quasar thus seems essential for ionizing gas at large distance from the nucleus.

**Narrow line quasars** In examining the quasar spectral characteristics, we note that 5 quasars (HE 0132-4313, HE 0450-2958, HE 1009-0702, HE 1228+0131 and HE 2258-5524) are fulfilling the Narrow Line Seyfert 1 (NLS1) criteria, i.e.  $\text{FWHM}(\text{H}\beta) < 2000 \text{ km s}^{-1}$ , strong FeII multiplets and  $[\text{OIII}]/\text{H}\beta < 3$  (Bian et al. 2004), even if their luminosities are characteristic of quasars and not of Seyferts. We call them "Narrow Line QSOs" (NLQSOs), with similar properties as NLS1s but at higher luminosities (as suggested by Stepanian et al. 2003). The proportion evaluated from optically selected samples amounts to 10 % only (Grupe et al. 2004), while it reaches 25 % here, although our sample is also optically selected. There was no selection bias on the spectral properties of the objects, but we have only 6 quasars with obvious broad components ( $\text{FWHM}(\text{H}\beta) > 4000 \text{ km s}^{-1}$ ), while the rest of the sample (9 objects) has hydrogen lines of intermediate widths. A deeper investigation of spectra in the whole HES survey reveals that 11 per cent of the quasars have  $\text{FWHM}(\text{H}\beta) < 2000 \text{ km s}^{-1}$ , as in other optically selected samples. However, the FWHM measurements are highly sensitive to spectral resolution and S/N (lower in HES than in this present study), and only one of the 5 NL objects of the present sample would be classified as such from the original HES spectra. The actual proportion of NLQSOs is thus probably higher than 11 per cent in HES, and this argument might also hold for other optical surveys.

The low-redshift QSO sample in HES is purely colour-selected, and there is no reason why the sample might be biased in favour of narrow-line QSOs. We note that the distribution of  $\text{H}\beta$  linewidths in the HES is strongly peaked with a mode of about  $2700 \text{ km s}^{-1}$  and a median of  $2940 \text{ km s}^{-1}$ , which is not much more than the conventional NLS1 criterion of  $2000 \text{ km s}^{-1}$ . Inspection of the spectra of objects close to this limit confirms that it is not a physically meaningful separation of distinct quasar sub-populations. For instance, we could add 4 more NL candidates in our sample if the limit was situated at  $2300 \text{ km s}^{-1}$  rather than  $2000 \text{ km s}^{-1}$  (all quasars but one presenting prominent iron lines have a  $\text{H}\beta$  FWHM close to this limit), reinforcing our suggestion that the present NLQSO classification is largely arbitrary. The median  $\text{FWHM}(\text{H}\beta)$  of our sample is  $2500 \text{ km s}^{-1}$ , which is fully compatible with the full HES sample. We conclude that our sample is a fair subset of the low-redshift quasar population. It should however be pointed that the mean  $\text{FWHM}(\text{H}\beta)$  of the HES sample is substantially lower than found in the SDSS quasars ( $\sim 5300 \text{ km s}^{-1}$ ) of the same luminosity and mass range (Schneider et al. 2005). The reason for that difference is not known.

The host of those five NLQSOs span the whole range of magnitudes of our sample, 2 out of 5 are interacting, 3 have undefined morphology (2 with intermediate-age stellar population, 1 undefined), one is a spiral and one an elliptical. The nucleus-to-host luminosity ratio estimated from images ranges between 3 and 18, except for the peculiar HE 0450-2958 described in Magain et al. (2005) for which the upper limit on host magnitude gives a minimum N/H of 85. Mass modelling (Section 8.1), applied to two of the NLQSOs reveals neither under- nor over-massive hosts compared to broad line QSOs. There is thus no clear tendency for NLQSOs to appear in a special type of host galaxy.

## 9.2 Central mass

There exists a widely used relation between the black hole mass ( $M_{\text{BH}}$ ) and characteristics of the Broad Line Region of quasars (Kaspi et al. 2000):

$$M_{\text{BH}} = R_{\text{blr}} v_{\text{blr}}^2 G^{-1} \quad (2)$$

This virial black hole mass estimate relies upon the hypothesis that dynamics in the BLR is dominated by gravitation. The reverberation mapping method has allowed to measure directly the radius  $R_{\text{blr}}$  of the BLR in several active nuclei, and a correlation has been found between  $R_{\text{blr}}$  and the AGN luminosity at 5100 Å. The velocity dispersion  $v_{\text{blr}}$  is estimated from the FWHM of the broad component of H $\beta$ .

In a significant fraction of our quasars, it is however problematic to estimate accurately the width of the broad part of the hydrogen line. When the narrow component cannot be clearly detected and when the broad H $\beta$  itself tends to be rather narrow, the separation between both components depends highly on assumptions that are made on flux ratio between [OIII] 5007 Å and the narrow H $\beta$  line, or on the adopted fixed width for this narrow component (see for instance Grupe et al. 2004). Here we choose to present mass estimates including global FWHM(H $\beta$ ) when the separation is not straightforward, assuming that in these cases the contribution of the narrow component is negligible. In parallel, we evaluate the uncertainty on these values by making a second determination based on the assumption that the narrow H $\beta$  has the same width as [OIII] 5007 Å in order to separate the former from the broad component. This uncertainty on narrow/broad line decomposition will mainly affect the quasars with the narrowest lines, thus the lowest black hole masses, which might thus be underestimated.

Figure 16 shows histograms of black hole masses using the regression from Kaspi et al. (2000), after conversion of our luminosities to their cosmology ( $H_0 = 75 \text{ km s}^{-1} \text{ Mpc}^{-1}$ ,  $\Omega_m = 1$  and  $\Omega_\Lambda = 0$ ). We find that interacting systems are hosting slightly more massive black holes (on average, in solar masses,  $\log M_{\text{BH}} = 8.1 \pm 0.6$  in interacting hosts and  $\log M_{\text{BH}} = 7.9 \pm 0.5$  for isolated ones).

This observation of higher mass black holes in currently interacting systems is somewhat surprising. One might expect that the central mass grows during the merger process and thus reaches higher masses when the system has had time to relax. Those massive black holes might however be the result of previous mergers, being in more crowded neighbourhoods, which would also explain the presence of large amounts of gas. However, the incomplete analysis of the neighbourhood made with the slits available (Section 8.2) does not allow to give a clear answer to this question. Another possible explanation is that there exist several scenarios to feed and trigger the quasars, the most efficient being a merger, creating the most massive black holes, while lower mass black holes would follow another evolution scheme (see Section 7.4).

Figure 16 also suggests that there is a trend for spirals to host less massive black holes. This is consistent with the idea that mergers bring fuel to the nucleus. Those disc galaxies have not yet undergone major interactions, as mergers would have produced larger spheroids (Stanford & Bushouse 1991).

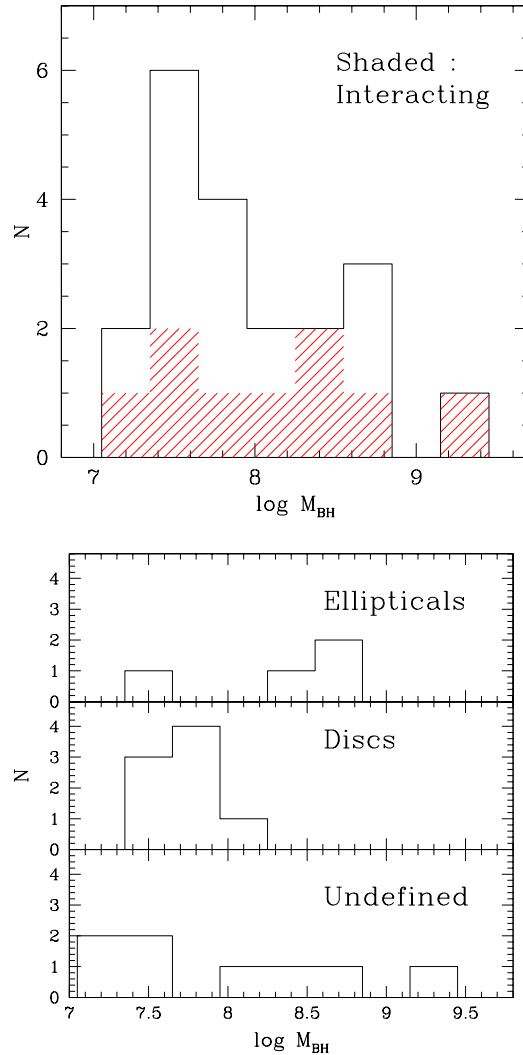


**Figure 16.** Histogram of the black hole masses found with the virialized BLR method. *Top:* global histogram where the black holes hosted in interacting system are shaded. *Bottom:* histograms of  $M_{\text{BH}}$  as a function of morphological classification.

## 9.3 Accretion rates

The nuclear luminosity measured on quasar spectra can provide direct indications on accretion rates in the nucleus, as  $\dot{M} = L/\eta c^2$ , where  $L$  is the bolometric luminosity of the quasar and  $\eta$  is the efficiency of the energy transfer from mass falling to the black hole, that we assume to be constant. The observed bolometric luminosity is estimated from the optical monochromatic luminosity:  $L_{\text{obs}}^{\text{bol}} \sim 10\lambda L_{5100}$  (Laor et al. 1997). In Fig. 17 we compare  $L_{\text{obs}}^{\text{bol}}$  to the Eddington bolometric luminosity  $L_E$ , i.e. the maximum luminosity of a source that is powered by spherical accretion.  $L_E$  was estimated from  $M_{\text{BH}}$  following Eq. 3, stating equilibrium between radiation pressure and gravitation:

$$L_E = 1.26 \cdot 10^{38} (M_{\text{BH}}/M_\odot) \text{ erg s}^{-1} \quad (3)$$

From Figs. 17 and 18 it appears that four quasars may be accreting above the Eddington limit. These ones are indeed among the NLQSOs discussed in Section 9.1. Those objects may be considered as active nuclei in an early stage

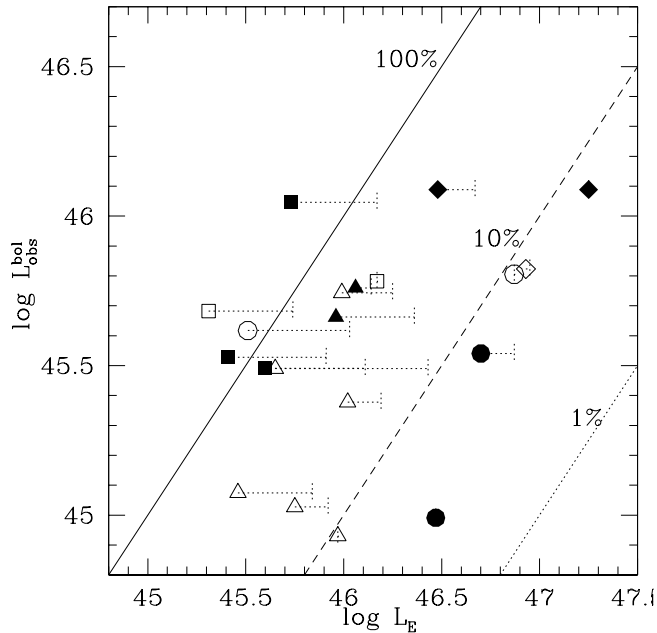


**Figure 17.** Observed nuclear luminosity versus Eddington luminosity evaluated from the BH mass. The dotted, dashed and solid lines are at 0.01, 0.1 and 1 Eddington luminosity, respectively. The one-sided error bars show where the objects would lie if we had separated the broad and narrow H $\beta$  as explained in the text. Symbols are as in Fig. 15: filled symbols for hosts with interaction, morphology of the galaxies identified by triangles for discs, circles for ellipticals, squares when undefined and diamonds for undefined with young population.

of activity. The accretion rates are high while the black holes are not very massive yet, and those rates probably fall to sub-Eddington ratios after a short period of activity. This observation is however highly sensitive to the definition of the broad H $\beta$  component. If we had chosen to separate the broad and narrow components of the hydrogen line as sketched in the previous subsection, no quasar would have been found with super Eddington luminosity or accretion rate, as shown in Fig. 17 by the dotted error bars and in Fig. 18, bottom. As can be seen from these figures, the objects most sensitive to this effect are the ones with narrow H $\beta$ , thus potentially super Eddington. This points once more to the ambiguity of the classification and interpretation of the Narrow Line AGN phenomenon.

The mean accretion rate for quasars in interacting systems is  $0.64 \dot{M}_E$  while it is  $0.58 \dot{M}_E$  for non interacting ones ( $\dot{M}_E$  being the Eddington accretion rate). If we adopt a typical value for the efficiency  $\eta = 0.1$ , these accretion rates translate to  $\dot{M} = 0.67 \pm 0.39 M_\odot \text{yr}^{-1}$  for non interacting and  $\dot{M} = 1.11 \pm 0.77 M_\odot \text{yr}^{-1}$  for interacting hosts.

From these estimates and from Fig. 18 which shows the accretion rate plotted versus BH mass, it appears that on average the accretion rate is larger when there is gravitational interaction, and that for a given central mass, the Eddington ratio is higher in interacting systems. In contrast, isolated spiral galaxies have, on the average, lower accretion rates onto lower mass BHs (as confirmed by Fig. 16). This is also coherent with the BH-mass/bulge-mass relation (e.g.

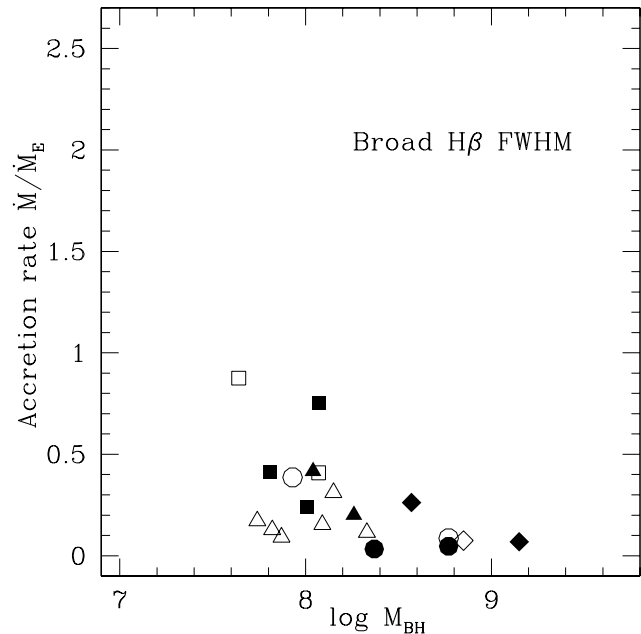
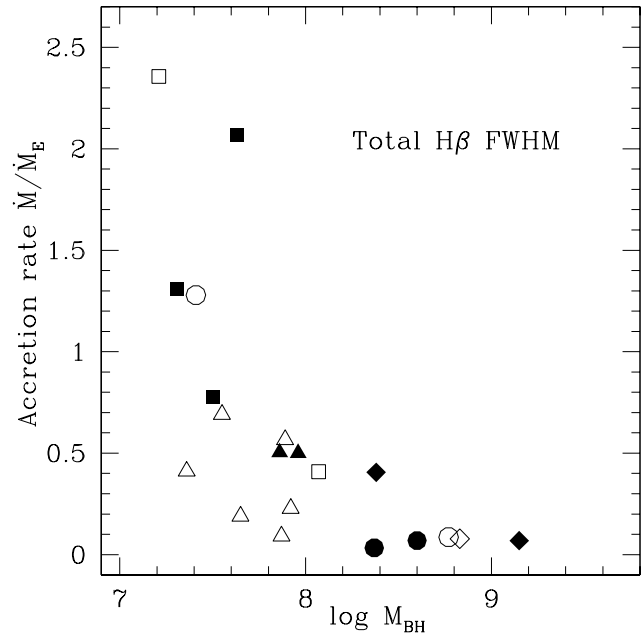


**Figure 18.** Accretion rate in unit of  $\dot{M}_E$  versus black hole mass in  $M_\odot$ . Both values depend on the estimation of FWHM(H $\beta$ ). Symbols are as in Fig. 15. *Top*: estimates from the total H $\beta$  FWHM. *Bottom*: estimates from the FWHM of the broad H $\beta$  only, after subtracting a narrow component of the same width as the [OIII] line.

Marconi & Hunt 2003), spirals having smaller bulges than ellipticals.

Figure 18 can be interpreted as showing the evolution of the quasar during its lifetime. A young nucleus has high accretion rate and low-mass black hole, that progressively grows while the accretion rate reduces. Two such sequences might be found in Fig. 18. First, at the bottom left, isolated spirals leading to moderate BHs ( $\sim 10^8 M_\odot$ ). Secondly, at higher accretion rates, system undergoing strong gravita-

tional interactions, leading to elliptical hosts with massive central BHs.

## 10 REDSHIFT DETERMINATION

Analyses of quasar emission lines show, as already observed for instance by Eracleous & Halpern (2004) and Boroson (2005), that narrow lines such as [OIII] are generally blueshifted relative to broad hydrogen lines. The question then is to know which lines are most suitable for measuring the actual redshift of the whole object. The availability of accurate symmetrical rotation curves in our sample provides a good opportunity to answer this question. Taking advantage of the separation we are able to make between nucleus and host emission lines, we have computed accurate redshifts for those galaxies which show the most regular rotation curves (HE 0132-4313, HE 0914-0031, HE 1009-0702, HE 1503+0228 and HE 2345-2906), averaging shifts from points of the extracted rotation curves symmetrical around the centre. After that, we have searched in the quasar spectra which lines provides the best estimator of the host galaxy redshift. For all five of them, it is the wavelength corresponding to the tip of the H $\alpha$  line which best matches the galactic redshift (within 0.2 Å, or a fifth of a pixel), followed with nearly the same accuracy by the H $\beta$  tip. The observed shifts are summarized in Table 9. Assuming those 5 objects are representative of undisturbed quasar host galaxies and that the quasar is motionless in the galaxy, we conclude that the tips of the quasar H $\alpha$  and H $\beta$  lines provide the best indicators of galactic redshift. Variations of redshifts in the quasar emission lines can thus be interpreted as bluer or redder in comparison with the global object velocity and not only in between each other. The redshifts measured from the position of the H $\alpha$  tip for the whole sample are presented in Table 1.

## 11 COMMENTS ON INDIVIDUAL OBJECTS

- HE 0132-4313: Host galaxy with undefined morphology and intermediate age stellar population. No sign of interaction. Quasar spectrum typical of Narrow Line Quasar (NLQSO).

- HE 0203-4221: This object shows all signs of merger-induced and enhanced activity: high ionization level found locally in the galaxy, young stellar population, evidence for interaction from significant distortions in the image and radial velocity curve.

- HE 0208-5318: Normal disc-like stellar population, no sign of interaction and gas metallicity indicative of weakly enriched medium.

- HE 0306-3301: Spiral galaxy with highly disturbed rotation curve, as a likely sign of interaction. Young stellar population and low metallicity.

- HE 0354-5500: Merger in a spiral galaxy, inducing high level ionization and asymmetric rotation curve.

- HE 0441-2826: Stellar content typical of disc. No information from acquisition image (saturated quasar), but radial profile pointing to elliptical morphology from a previous NIR study (Kuhlbrot 2003). No extended emission line suitable for radial velocity curve extraction. It is the only object

with a clear mismatch between stellar population (young) and morphology (elliptical). The gas metallicity also points to a low enrichment by stars. The quasar spectrum itself is peculiar, with broad H $\beta$  blueshifted with respect to the narrow component ( $\sim 2700 \text{ km s}^{-1}$ ), probably revealing an outflow. Traces of shells or interaction would not be surprising if high resolution imaging was available.

- HE 0450-2958: This object is a special case that has been addressed by Magain et al. (2005). Upper limits were placed on the undetected stellar contribution to the spectrum of the host, and only a cloud of gas ionized by the quasar was detected. As there is no detection of any host, this object is not included in global means or detailed galactic component analysis. Quasar spectrum typical of NLQSO.

- HE 0530-3755: One of the faintest hosts detected in the sample, but with a high Balmer decrement on quasar broad lines that might suggest obscuration by dust on the nucleus and for the host as well. Small amount of gas partially ionized by the quasar; images suggesting interaction with tidal tail to the West, one close companion at 6 arcsec East, that luckily partially falls on the slit and whose spectrum shows nearly identical redshift (faint galaxy, low continuum and only H $\alpha$  detected in emission), plus another putative companion 9 arcsec South. The nucleus has an accretion rate above the Eddington limit, but without matching all the NLQSO criteria.

- HE 0914-0031: Normal spiral galaxy with high mass-to-light ratio according to the mass modelling of Section 8.1.

- HE 0956-0720: Bad PSF, inducing poorly deconvolved spectrum. No interpretation possible with such a low S/N. Morphological classifications from previous studies are contradictory (Kuhlbrot 2003, Percival et al. 2001).

- HE 1009-0702: Normal late-type spiral galaxy according to morphology, stellar and gaseous content. Quasar spectrum typical of NLQSO.

- HE 1015-1618: Poor separation from the quasar because of a bad PSF.

- HE 1029-1401: The lowest redshift object of the sample, luminous elliptical with minor mergers, already considered in several previous studies. Gas highly ionized by the nucleus.

- HE 1228+0131: Poor separation of the host from the quasar, because the saturation level of the detector was almost reached. No interpretation possible. Quasar spectrum typical of NLQSO.

- HE 1302-1017 (or PKS 1302-102): This object is the only radio loud quasar in the sample. It cannot be properly classified concerning morphology. Bahcall et al. (1997) classify the host as elliptical because of its smooth and elliptical shape from *HST* imaging, although they find an exponential profile to fit their data slightly better. In Kuhlbrot (2003) it is classified as disc from 2D modelling on NIR images, but presents an irregular radial profile. It is the most luminous object of the sample. The stellar population of the host galaxy is typical of Sc disc population. It has low gas metallicity and the highest SFR of the HII subsample. From Bahcall et al. (1997), it has two small companions merging in, perturbing the radial velocity curve presented in this paper and probably explaining the irregular radial profile, but without high excitation of the large amount of gas present in this host. If it is a morphologically disc-dominated galaxy, the stellar and gaseous analyses point

**Table 9.** Observed shifts of the main quasar emission lines relative to the galactic lines, expressed in  $\text{km s}^{-1}$ . Each line position is estimated by a gaussian profile fitting (first line, *g*) and from the wavelength corresponding to the tip (maximum intensity, second line, *t*).

|                       | HE 0132-4313 | HE 0914-0031 | HE 1009-0702 | HE 1503+0228 | HE 2345-2906 | Mean shift | $\sigma$ |
|-----------------------|--------------|--------------|--------------|--------------|--------------|------------|----------|
| H $\alpha$ (g)        | +22          | -104         | -97          | -117         | -52          | -70        | 41       |
| H $\alpha$ (t)        | +7           | -3           | +7           | +4           | -30          | -3         | 16       |
| H $\beta$ (g)         | 0            | +5           | -189         | -133         | -40          | -71        | 84       |
| H $\beta$ (t)         | +5           | +5           | +24          | +4           | -35          | +1         | 21       |
| OIII <sub>1</sub> (g) | -            | -27          | -            | -85          | -109         | -74        | 42       |
| OIII <sub>1</sub> (t) | -            | -9           | -            | -91          | -99          | -66        | 50       |
| OIII <sub>2</sub> (g) | -            | -27          | -            | -79          | -103         | -70        | 39       |
| OIII <sub>2</sub> (t) | -            | -5           | -            | -79          | -98          | -61        | 49       |

to Sc-Sd where merger-induced star formation and activity appear, giving a counter-example of a luminous radio-loud quasar not hosted by an elliptical. On the other hand, if it is an elliptical galaxy, it must anyway have undergone recent mergers, which have largely enhanced star formation and brought a large amount of fresh gas, able to mask the old stellar populations from our analyses.

- HE 1434-1600: Elliptical galaxy with gas ionized by the quasar at large distance from the nucleus, discussed in Letawe et al. (2004).

- HE 1442-1139: Probable S0-like galaxy, with no gas detected.

- HE 1503+0228: Normal spiral host galaxy, studied as a test case in Courbin et al. (2002).

- HE 2258-5524: Major merger resulting in highly ionized gas and asymmetric rotation curve. Stellar population typical of S0-Sa galaxy. Quasar spectrum typical of NLQSO.

- HE 2345-2906: Spiral host galaxy for one of the weakest quasars of the sample (at the limit of the quasar/Seyfert separation). The narrow lines in this the quasar are much more prominent relative to the broad components than for all other objects of the sample.

## 12 DISCUSSION

### 12.1 Quasar hosts characterization

A first striking result is that most quasar host galaxies harbour large amounts of gas (ionized by stars, by the AGN or marginally by shocks), irrespective of morphological type. We can thus safely reinforce the conclusions of Scoville et al. (2003), based on molecular CO detection, that high luminosity quasars are generally *not* found in normal (i.e. gas-poor) ellipticals. Previous mergers or collisions are probably the source of gas for ellipticals.

There is an obvious predominance of globally young stellar population (10/15 of the hosts with known stellar content). As several hosts with a young stellar population have unknown morphologies, this observation could be linked to the bluer colours of elliptical quasar hosts in comparison to inactive ellipticals found in several recent multicolour imaging studies (e.g. Kauffmann et al. 2003; Jahnke et al. 2004; Sanchez et al. 2004). We note that the two elliptical hosts for which our stellar population analysis shows a predominantly old population (HE 1434-1600 and

HE 1029-1401) are also presenting this type of bluer colours, according to Jahnke et al. (2004). One thus has to conclude that they contain a globally old stellar population, as deduced from Lick indices analyses, over which appears an additional fraction of younger stars which account for the blue colour excess, without significantly modifying the spectral absorption diagnostics of section 7.1. As the bluer-than-expected ellipticals display a globally old stellar population with an additional young component, and as most of the host galaxies with a globally young stellar population are disc-dominated, we can probably conclude that most of the hosts with undefined morphologies and young stellar population have a significant disc component.

From a statistical point of view, the proportion of discs found in this study (8 of the 19 radio quiet quasars, or 7/14 if we remove the NLQSOs that are often excluded from quasar samples, thus around 45 %) is compatible with the proportions found by Dunlop et al. (2003) and Floyd et al. (2004) (namely around 30 % among radio quiet quasars), given the limited number of objects in both samples. But as these last two studies have used several constraints on target selection, there might indeed be a selection bias in their samples towards ellipticals, while no other constraint apart from luminosity was applied to ours. Given that our proportion is a lower limit, the radio quiet quasars probably appear as often in spirals as in ellipticals.

The confirmed spirals show HII regions compatible with rather metal-poor Sc to Sd types, regarding star formation and gas metallicity. Their black holes are less massive than the ones found in ellipticals (as expected from the bulge mass - black hole mass scaling relation, McLure & Dunlop 2002), and only a minority present signs of interaction (2/8).

The elliptical host galaxies contain ionized gas (3/4), have massive black holes and at least 50 % of them present signs of interaction. The only *normal* elliptical, with no gas detected, could not be well deconvolved, so that no detailed analysis of its stellar and gas content has been possible.

It has been claimed that all quasars more luminous than  $M_V = -23.5$  are hosted by massive ellipticals (Dunlop et al. 2003; Floyd et al. 2004). Converting this limit to our cosmology gives  $M_V < -23.25$ . As seen from Table 1, all our quasars but one are brighter than this limit, and even if the most luminous AGNs lie in ellipticals, we find almost half of them inside disc-dominated galaxies in this magnitude range. The mean nuclear *V* magnitudes are  $M_V = -24.5$

both for elliptical and for disc hosts, even if we remove the potential NLQSOs identified as discs from our sample (they were excluded from Dunlop's sample). This observation that the morphology of luminous quasar host galaxies are not necessarily elliptical was also put forward by Sanchez et al. (2004) in the case of higher redshift quasars ( $0.5 < z < 1.1$ ).

## 12.2 The quasar-host connection

### 12.2.1 Influence of galactic environment on the activity of the nucleus

As shown in Section 9, interaction obviously brings material (gas, and probably dust) to the central part of the galaxy and enhances the accretion rate and power of the quasar. Recent simulations of galaxy mergers (Di Matteo et al. 2005; Cattaneo et al. 2005) lead to the same conclusions. The most massive black holes are hosted in systems presently interacting, while we might have expected them in systems at the end of the merging process, as discussed in Section 9.2. The quasar harboured by interacting systems are also more powerful.

On the other hand, half of our quasars are found in non-interacting galaxies, with a majority of spiral hosts (6 confirmed discs, 2 ellipticals and 3 undefined). Most of them are young gas-rich systems. The predominance of a disc component ensures that these system have not undergone major mergers, as the latter tend to produce spheroids (Stanford & Bushouse 1991).

This suggests that mergers are not the only mechanism for triggering activity, as already proposed by Jahnke et al. (2004) and Dunlop et al. (2003). Alternative mechanisms may be bar-driven accretion (found to be very efficient for AGN fueling for instance in NLS1s, Crenshaw et al. 2003, or for HE 2345-2958 in the present study) or gravitational instabilities related to spiral arms formation. But small scale nuclear events, related to an early stage of formation of spiral galaxies, might also trigger activity. They are undetectable with the spatial resolution of the present observations. Galactic winds arising from central supernovae are plausible drivers of fuel towards the central engine, given that the weak enrichment of gas in heavy elements is measured on global spectra only.

There does not seem to be a single scenario for the evolution of quasars and their hosts, but different evolution schemes lead to different characteristics of the central engine. If the system encounters major merger events, it will lead to a higher BH mass and a more powerful nucleus, but the nucleus could be active as well with less dramatic and smaller scale events in young spiral galaxies, leading to smaller and less powerful quasars.

### 12.2.2 Influence of the quasar radiation on the host galaxy

In 7 galaxies out of 20, we find gas ionized by the quasar far from the nucleus (in ellipticals, spirals or undefined hosts). This phenomenon is independent from radio emission, as none of the objects with such long-range ionization is radio loud. The common characteristics of those galaxies are of course the presence of gas, but also a powerful quasar, and evidences for gravitational interaction, two properties that are linked. The origin of high ionization may lie in the fact

that gas and dust around the nucleus are swept by the interaction and let the powerful nuclear ionizing beam reach large distances throughout the galaxy.

The analysis of gas metallicity in quasar hosts with a HII region-like ISM shows abundances at the lower end of typical spiral metallicities. The nuclear activity in these young systems could slow down the star formation efficiency in some way, hampering the formation of massive stars and slowing down the enrichment of the surrounding gas. Links between star formation and quasar activity (Jahnke et al. 2004) are preferentially found for elliptical hosts where activity seems to enhance star formation. However, in that case, neither quasar activity nor star formation would be expected in an isolated host. Both are made possible by the presence of gas, probably brought by mergers with younger systems. We agree with the conclusions of Canalizo & Stockton (2001) who, from a study of UltraLuminous IR Galaxies and QSOs, conclude that it is the merging process that triggers both star formation and activity, without finding evidence for any direct influence from one of these onto the other. In contrast, it does not appear unrealistic to suggest that the quasar activity might slow down the star formation in young, isolated, gas-rich spiral galaxies.

Further spectroscopic and high resolution imaging investigations of larger samples of quasars and their hosts could allow to confirm the trends found here and allow a sharper tuning of the interpretations and hypotheses on the quasar ignition and evolution.

## ACKNOWLEDGMENTS

G. L. is a teaching assistant supported by the University of Liège, (Belgium) . The Pôle d'Attraction Interuniversitaire, P5/36 and PRODEX 90195 (PPS Science Policy, Belgium, and ESA) contracts are thanked for financial support. F. C., P. J. and G. M. acknowledge support from the Swiss National Science Foundation. K. J. was supported by the German DLR under project number 50 OR 0404 and DFG project SCHI 536/3-1.

## REFERENCES

- Bahcall J.N., Kirhakos S., Saxe D.H., 1997, ApJ, 479, 642
- Baldwin J., Phillips M., Terlevich R., 1981, PASP, 93, 5
- Bian W., Zhao Y., 2004, MNRAS, 352, 823
- Boroson T. A., Oke J. B., 1984, ApJ, 281, 535
- Boroson T., Persson S., Oke J., 1985, ApJ, 293, 120
- Boroson T. A., 2005, AJ, 130, 381
- Canalizo G. & Stockton A., 2001, ApJ, 555, 719
- Cardiel N, 1999, PhD Thesis, Universidad Complutense de Madrid
- Cattaneo A., Combes F., Colombi S., Bertin E., Melchior A.-L., 2005, MNRAS, 359, 1237
- Courbin F., Magain P., Kirkove M., Sohy S., 2000, ApJ, 539, 1136
- Courbin F., Letawe G., Magain P., Wisotzki L., Jablonka P. et al., 2002, A&A, 394, 863

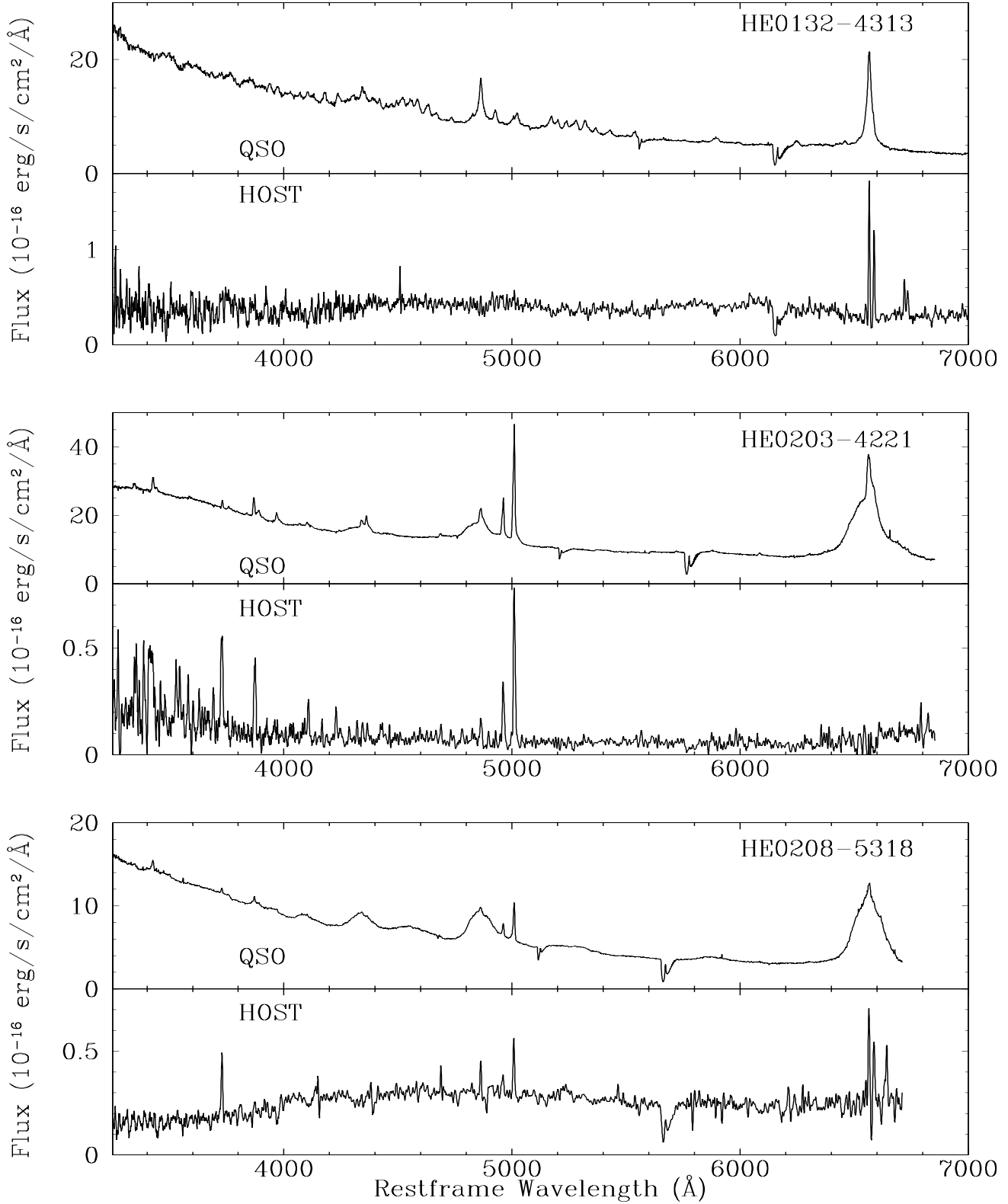


**Figure 19.** For each object, integrated spectra of the quasar-only on top and galaxy-only at the bottom, after deconvolution and separation, sorted by increasing right ascension. The dotted galactic spectra give the limits of over- and under- subtraction of the nuclear component as discussed in Section 4.1.

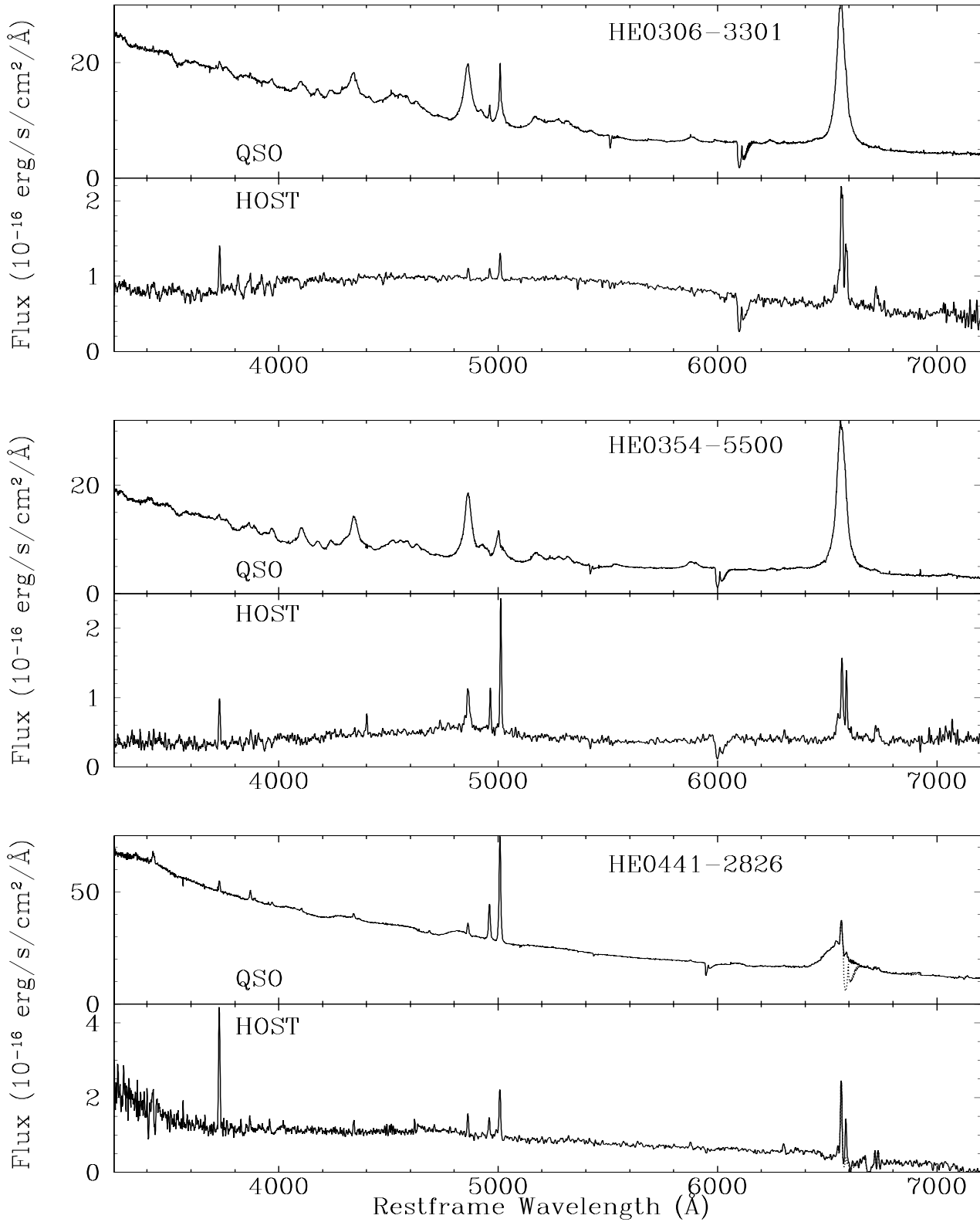


**Figure 19 – continued** There seems to be residual nuclear light in the continuum of the galaxy of HE0441-2826, because of a poorer PSF. The blend of H $\alpha$  with atmospheric absorption (dotted line) was partially corrected.



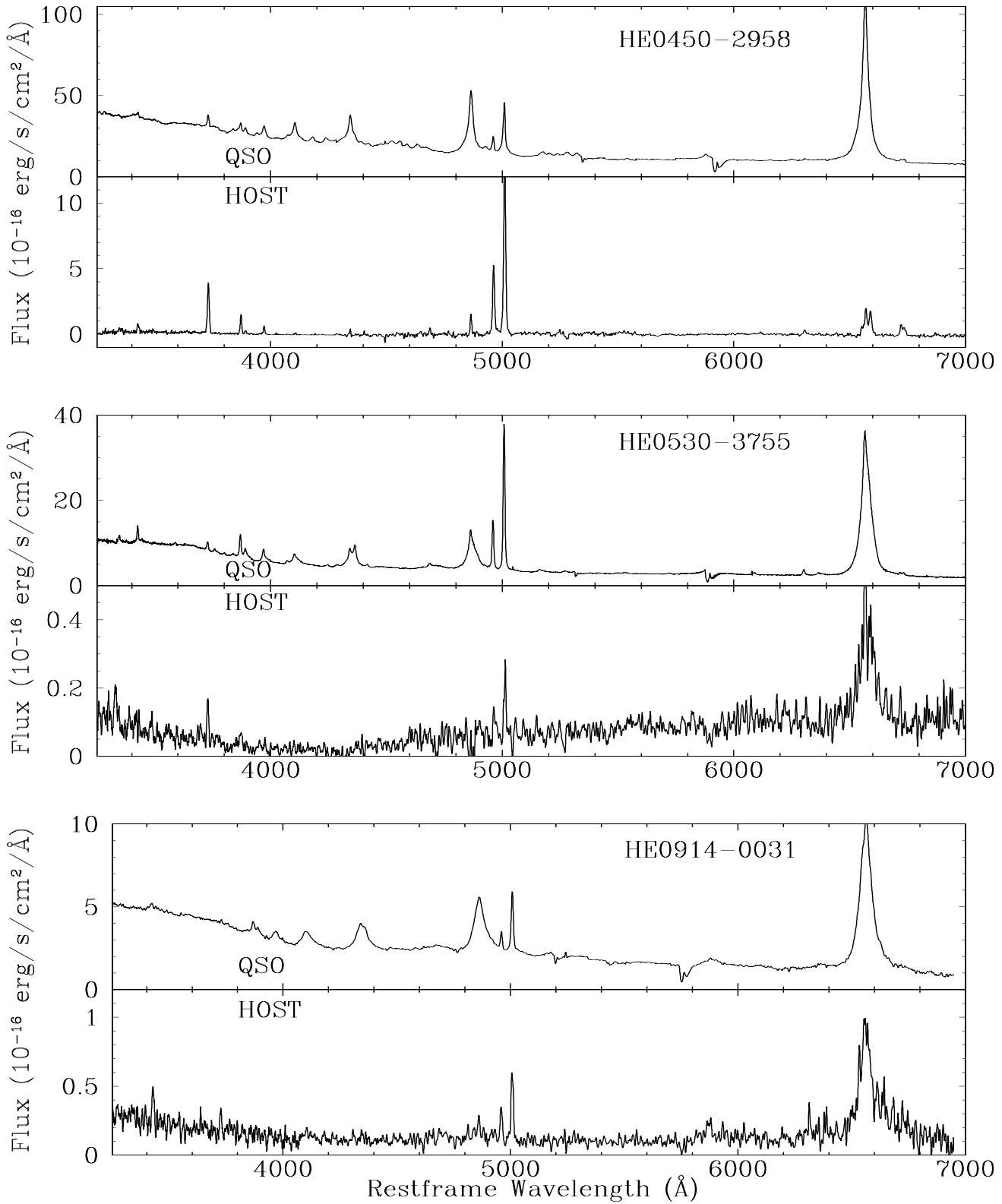
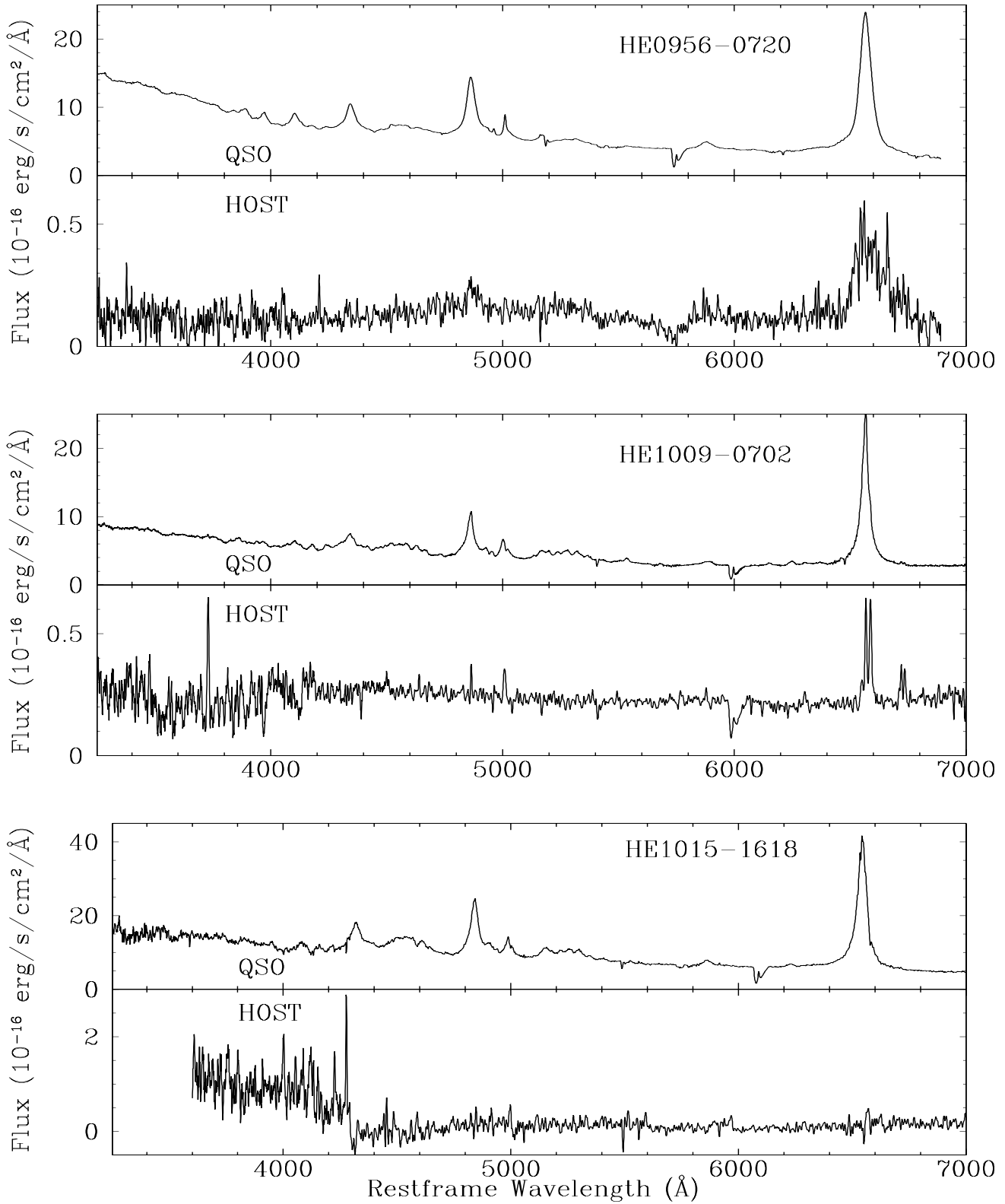
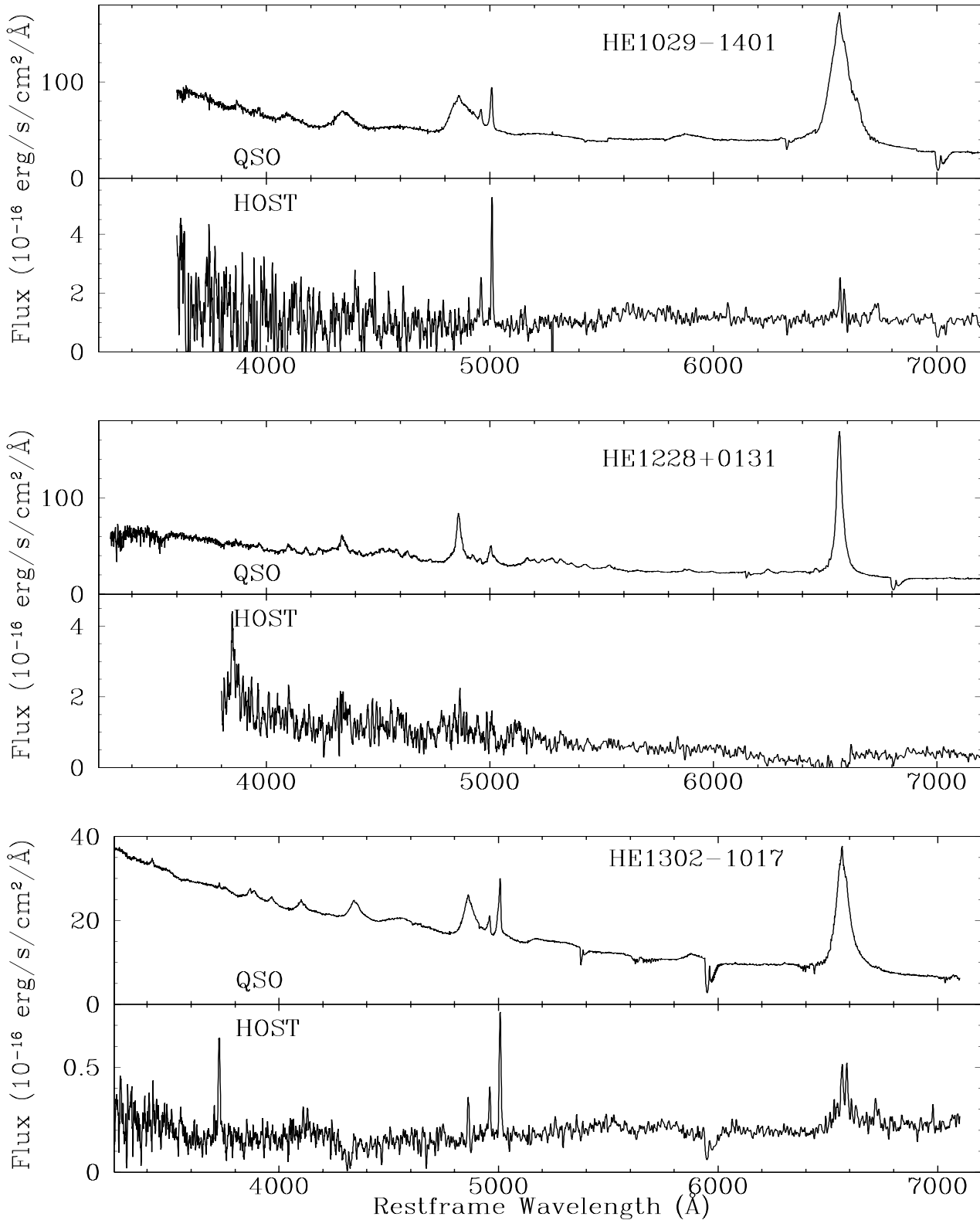


Figure 19 – continued Note the absence of continuum in the host of HE0450-2928.



**Figure 19** – *continued* HE0956-0720 and HE1015-1618 could not be properly deconvolved, because of high N/H and difficult PSF construction.



**Figure 19 – continued** Important noise in the bluer parts of the two first objects, the PSF stars being too faint in the blue for accurate deconvolution in this wavelength range. HE1228+0131 observations were near saturation level on the detector, leading to non adequacy of the PSF and thus poor deconvolution.

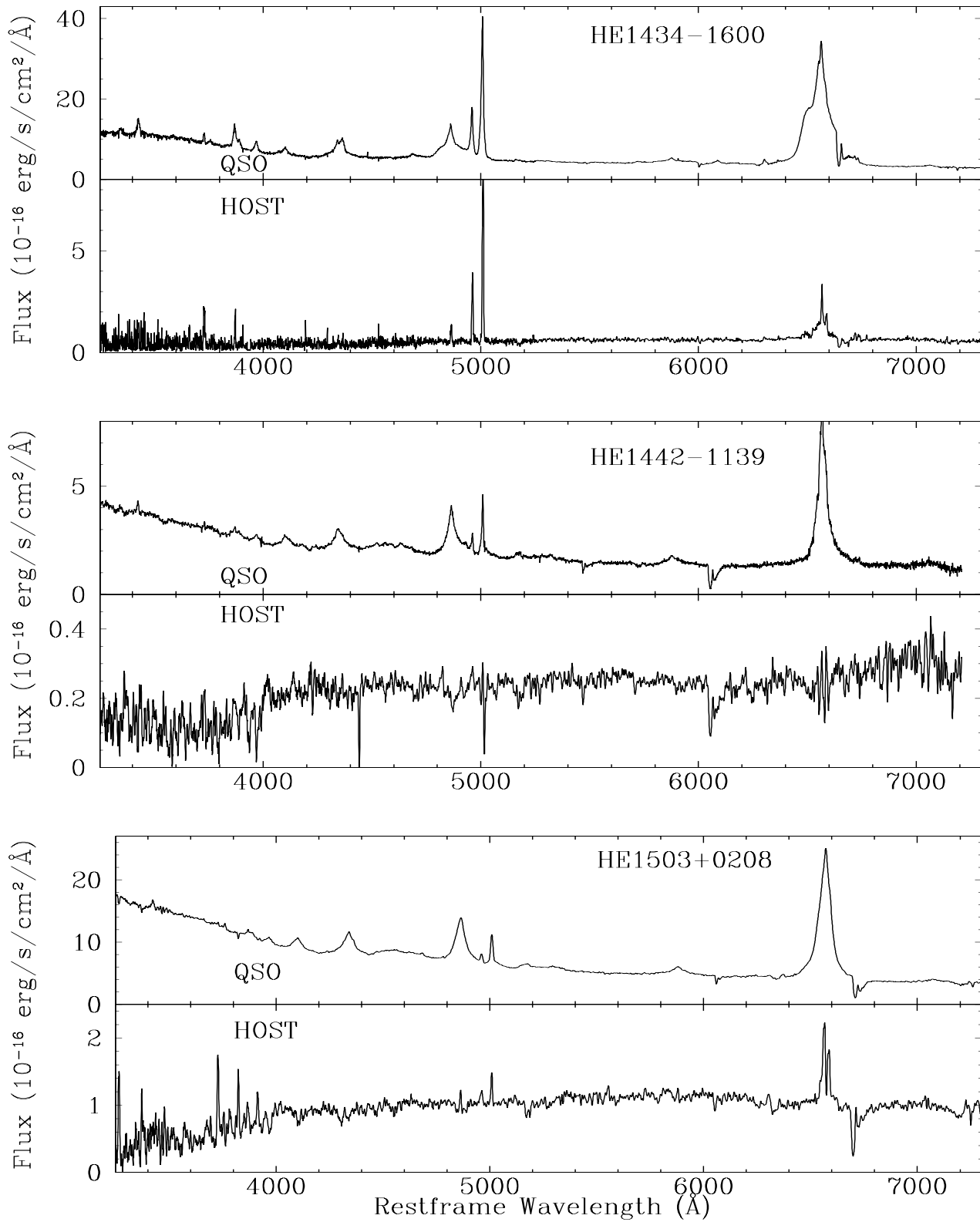


Figure 19 – *continued*

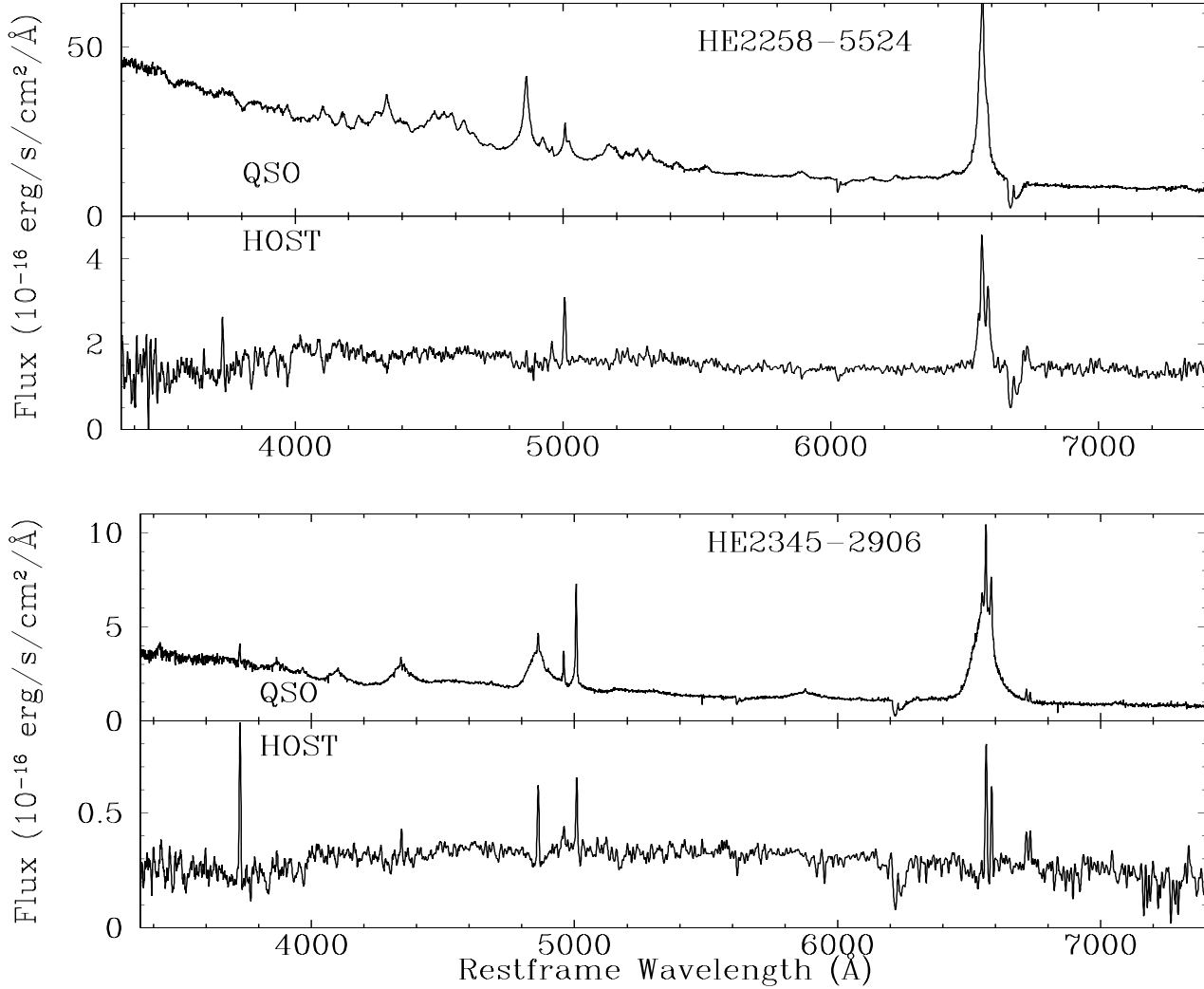


Figure 19 – continued

Crenshaw D.M., Kraemer S.B., Gabel J.R., 2003, *AJ*, 126, 1690  
 Di Matteo T., Springel V., Hernquist L., 2005, *Nature*, 433, 604  
 Dunlop J.S., McLure R.J., Kukula M. J., Baum S.A., O’Dea C.P. and. Hughes D.H., 2003, *MNRAS*, 340, 1095  
 Eracleous M., Halpern J.P., 2004, *ApJSS*, 150, 181  
 Evans I., Koratkar A., Allen M., Dopita M., Tsvetanov, Z. 1999, *ApJ*, 521, 531  
 Floyd D.J., Kukula M. J., Dunlop J.S., McLure R.J., et al. 2004, *MNRAS*, 355, 196  
 Francis P.J., 1996, *PASA*, 13, 212  
 Greenstein J.L., Schmidt M., 1964, *ApJ* 140, 1  
 Grupe D., Wills B.J., Leighly K.M., Meusinger H., 2004, *AJ*, 127, 156  
 Hutchings J.B., Crampton D., 1990, *AJ*, 99, 37  
 Hutchings J.B., Neff S.G., 1992, *AJ*, 104, 1  
 Izotov Y., Thuan T., 1999, *ApJ*, 511, 639  
 2003, *AJ*, 126, 63  
 Jahnke K., 2002, Doctoral Dissertation, Universität Hamburg  
 Jahnke K., Kuhlbrodt B., Wisotzki L., 2004, *MNRAS*, 352, 399  
 Jansen R.A., Fabricant D., Franx M., Caldwell N., 2000, *ApJSS*, 126, 331  
 Kaspi S., Smith P.S., Netzer H., Maoz D., Jannuzi B.T., Giveon U., 2000, *ApJ*, 533, 631  
 Kauffmann G., Heckman T.M., Tremonti C., Brinchmann J., Charlot S., White S.D., Ridgway S.E. et al., 2003, *MNRAS*, 346, 1055  
 Kennicutt R.C., 1992a, *ApJS* 79, 255  
 Kennicutt R.C., 1992b, *ApJ*, 388, 310  
 Kennicutt R.C., 1998, *ARAA*, 36, 189  
 Kewley L.J., Geller M.J., Jansen R.A., 2004, *AJ*, 127, 2002  
 Kewley L.J., Jansen R.A., Geller M.J., 2005, *PASP*, 117, 227  
 Kobulnicky H.A., Kennicutt R.C., Pizagno J.N., 1999, *ApJ*, 514, 544  
 Kobulnicky H.A., Phillips A.C., 2003, *ApJ*, 599, 1031  
 Kuhlbrodt B., 2003, Doctoral Dissertation, Universität Hamburg  
 Laor A., Fiore F., Elvis M., Wilkes B.J., McDowell J.C., 1997, *ApJ*, 477, 93

- Letawe G., Courbin F., Magain P., Hilker M., Jablonka P. et al., 2004, *A&A*, 424, 455
- Magain P., Courbin F., Sohy S., 1998, *ApJ*, 494, 452
- Magain P., Letawe G., Courbin F., Jablonka P. et al., 2005, *Nature*, 437, 381
- Maier C., Lilly S., Carollo C., Meisenheimer K., Hippelein H., Stockton A., 2006, *ApJ*, 639, 858
- Marconi A., Hunt L.K., 2003, *ApJ*, 589, L21
- McLure, R. J. and Dunlop, J. S., 2002, *MNRAS*, 331, 795
- McGaugh, S., 1991, *ApJ*, 380, 140
- Miller J.S., Sheinis A.I., 2003, *ApJ*, 588, L9
- Miller J.S., Mathews W.G., 1972, *ApJ*, 172, 593
- Moustakas, J. & Kennicutt, R., 2005, preprint, astro-ph/0511731
- Nolan L.A., Dunlop J.S., Kukula M.J., Hughes D.H., Boroson T., Jimenez R., 2001, *MNRAS* 323, 308
- Oke J. B., 1963, *Nature* 197, 1040
- Percival W., Miller L., McLure R., Dunlop J., 2001, *MNRAS* 322, 843
- Rönnback J., van Groningen E., Wanders I., Örndahl E., 1996, *MNRAS* 283, 282
- Sanchez S.F., Jahnke K., Wisotzki L., McIntosh D.H., Bell E.F. et al., 2004, *ApJ*, 614, 586
- Schlegel D.J., Finkbeiner D.P., Davis M., 1998, *ApJ*, 500, 525
- Schneider D.P. et al., 2005, *AJ*, 130, 367
- Scoville N., Frayer T., Schinnerer E., Christopher N., 2003, *ApJ*, 585, L105
- Smith E.P., Heckman T.M., Bothun G.D., Romanishin W., Balick B., 1986, *ApJ*, 306, 64
- Stanford S.A., Bushouse H.A., 1991, *ApJ*, 371, 92
- Stepanian J.A., Benitez E., Krongold Y., Cruz-Gonzalez I., de Diego J.A. et al., 2003, *ApJ*, 588, 746
- Stockton A., MacKenty J.W., 1987, *ApJ*, 316, 584
- Stockton A., MacKenty J.W., Hu E.M., Kim T.-S., 2002, *ApJ*, 572, 735
- Trager S.C., Worthey G., Faber S.M. et al. 1998, *ApJS* 116, 1
- Trèvese D., Vagnetti F., 2002, *ApJ*, 564, 624
- Vanden Berk D.E., Shen J., Yip C., Schneider D.P., Connolly A.J., Burton R.E. et al., 2006, *AJ*, 131, 84
- Veilleux S., Osterbrock D., 1987, *ApJS*, 63, 295
- Wisotzki L., Christlieb N., Bade N. et al., 2000, *A&A* 358, 77
- Worthey G., Faber S.M., Gonzalez J.J., Burstein D., 1994, *ApJSS*, 94, 687